Structural insights into TRPV4-Rho GTPase signaling complex function and disease

Do Hoon Kwon[1,†], Feng Zhang[1,†], Brett A. McCray[2], Meha Kumar[2], Jeremy M. Sullivan[2], Charlotte J. Sumner[2,3] & Seok-Yong Lee[1,*]

Affiliations:

[1] Department of Biochemistry, Duke University School of Medicine, Durham, North Carolina, 27710, USA.

[2] Department of Neurology, Johns Hopkins University School of Medicine, Baltimore, Maryland, USA

[3] Department of Neuroscience, Johns Hopkins University School of Medicine, Baltimore, Maryland, USA

[†] These authors contributed equally.

*Correspondence to:

S.-Y. Lee

Email: seok-yong.lee@duke.edu

Telephone: 919-684-1005

Abstract

Crosstalk between ion channels and small GTPases is critical during homeostasis and disease[1], but little is known about the structural underpinnings of these interactions. TRPV4 is a polymodal, calcium-permeable cation channel that has emerged as a potential therapeutic target in multiple conditions[2-5]. Gain-of-function mutations also cause hereditary neuromuscular disease[6-11]. Here, we present cryo-EM structures of human TRPV4 in complex with RhoA in the apo, antagonist-bound closed, and agonist-bound open states. These structures reveal the mechanism of ligand-dependent TRPV4 gating. Channel activation is associated with rigid-body rotation of the intracellular ankyrin repeat domain, but state-dependent interaction with membrane-anchored RhoA constrains this movement. Notably, many residues at the TRPV4-RhoA interface are mutated in disease and perturbing this interface by introducing mutations into either TRPV4 or RhoA increases TRPV4 channel activity. Together, these results suggest that the interaction strength between TRPV4 and RhoA tunes TRPV4-mediated calcium homeostasis and actin remodeling, and that disruption of TRPV4-RhoA interactions leads to TRPV4-related neuromuscular disease, findings that will guide TRPV4 therapeutics development.

47 **Main**

48 Although typically considered part of distinct signaling pathways, functional interactions
49 between ion channels and small GTPases have been reported for over two decades and control a
50 range of fundamental processes including cell migration, tumor vascularization, smooth muscle
51 contraction, and mechanosensation, among others[1,12-16]. Insight into how this dynamic crosstalk is
52 achieved is limited by the absence of resolved channel-GTPase structures and structure-guided
53 functional studies.

54 TRPV4, expressed in the plasma membrane of a wide range of cell types, is a polymodal
55 ion channel whose gating is controlled by multiple endogenous and exogenous stimuli including
56 synthetic ligands, cell swelling, shear stress, and moderate heat[17-19]. TRPV4 mediates calcium
57 dependent regulation of vascular tone, osmoregulation, bone homeostasis, itch, adipose
58 thermogenesis, inflammation, and pulmonary and renal functions[2-4,20]. TRPV4 channel activation
59 is linked to numerous disease states: pulmonary edema and cancer metastasis, amongst other
60 diseases[5,21]. Furthermore, gain-of-function missense mutations cause TRPV4 channelopathies,
61 which are grouped into autosomal dominant neuromuscular disorders (Charcot-Marie-Tooth
62 disease type 2C and distal spinal muscular atrophies) and skeletal disorders (skeletal dysplasias
63 and osteoarthropathy)[6-8,11]. Notably, while skeletal dysplasia mutations are distributed throughout
64 the TRPV4 channel, neuromuscular disease-causing mutations (referred to hereafter as neuropathy
65 mutations) are primarily localized to a confined region of the N-terminal cytoplasmic domain. We
66 previously showed that the cytoskeleton remodeling small GTPase RhoA functionally interacts
67 with TRPV4[22], but this interaction appears to be perturbed by neuropathy-causing mutations
68 resulting in increased TRPV4 channel activity, cytoskeletal remodeling, and cell process
69 retraction[22]. Overexpression of RhoA suppresses wild type (WT) TRPV4 channel-mediated

calcium influx in cultured mouse motor neuron–neuroblastoma fusion (MN-1) cells in response to hypotonicity demonstrating its ability to modulate TRPV4 function (Fig. 1a,b) [22].

TRPV4 channel inhibition is a promising therapeutic strategy for multiple diseases and conditions[20,23]. Administration of TRPV4 antagonists improves outcomes in animal models of pulmonary edema, blood-retinal and blood-brain barrier breakdown, and peripheral neuropathy[24-26] and the orally bioavailable TRPV4 antagonist GSK2798745 (Fig. 1c) has been through clinical trials for pulmonary edema, chronic cough, and diabetic macular edema (NCT02119260, NCT02497937, NCT03372603, and NCT04292912)[23,24]. Understanding the structural bases of ligand-dependent TRPV4 gating as well as channel modulation by RhoA will enhance drug design for TRPV4-dependent diseases. To date, the only published structure of TRPV4 is from *Xenopus tropicalis* in its ligand-free, non-conducting state[27], but the atypical non-domain-swapped tetrameric channel arrangement calls into question its physiological relevance[28]. Therefore, little is known about the agonist- and antagonist-binding sites within TRPV4 and how they exert effects on channel gating.

Results

Structures of human TRPV4 in complex with RhoA

We expressed full-length WT human TRPV4 in HEK293S GnTi$^-$ cells. The protein was extracted and purified in detergent and the structure determined using single-particle cryo-electron microscopy (cryo-EM) (Figs. 1d-f). Surprisingly, although we overexpressed TRPV4 only, an additional protein density associated with each cytoplasmic domain of the tetrameric TRPV4 channel was resolved in the final three-dimensional (3D) reconstruction (Fig. 1d). The published RhoA crystal structure (PDB: 1FTN) fits reasonably well into this density, suggesting that endogenous RhoA was copurified with overexpressed TRPV4. The presence of RhoA in the final

94 purified TRPV4 samples was confirmed by Western blot using a RhoA-specific antibody
95 (Extended Data Fig. 1a). The C1-symmetric 3D reconstruction showed RhoA occupancy at all
96 four subunits of the TRPV4 homotetramer (Extended Data Fig. 1b). We define this ligand-free
97 TRPV4-RhoA complex structure as the apo state. Three additional complex structures were
98 determined in the presence of distinct ligands (Figs. 1c-f): the antagonist GSK2798745-bound
99 TRPV4-RhoA complex in the closed state, the agonist GSK1016790A-bound TRPV4-RhoA in
100 the open state, and the agonist 4α-phorbol 12,13-didecanoate-bound TRPV4-RhoA in the putative
101 open state (ligands are abbreviated as GSK279, GSK101, and 4α–PDD, respectively). The 3D
102 reconstructions of the four structures were resolved to 3.30 to 3.75 Å resolutions (Extended Data
103 Figs. 1c-h). Particle subtraction followed by focused 3D classification of the transmembrane
104 region and RhoA-bound cytoplasmic domain were performed in turn, resulting in improved map
105 qualities for these regions for model building (Extended Data Fig. 2). Although the EM density
106 for the pore domain in the apo state and the 4α–PDD-bound structures was resolved sub-optimally,
107 the high-quality reconstructions for the GSK279-bound closed state and the GSK101-bound open
108 state enabled us to unambiguously model the register and assign the gate residues (Extended Data
109 Fig. 3). Notably, we observed EM density of the RhoA C-terminus extending to the detergent
110 micelle that surrounds the TRPV4 transmembrane region, suggesting that the geranylgeranylated
111 C-terminus of RhoA anchors to the inner leaflet of the membrane bilayer and facilitates its
112 association with TRPV4 in the cellular context (Fig. 1g).

113 Human TRPV4 adopts a two-layered homotetrameric architecture where RhoA attaches to
114 the bottom layer. The top layer, or the transmembrane region, comprises the voltage-sensor-like
115 domain (VSLD) and the pore domain. The VSLD is formed by transmembrane helices S1 to S4,
116 while the pore domain contains the S4-S5 junction, S5, the pore helix (PH), the selectivity filter
117 (SF), the pore loop, the pore-lining helix S6, and the TRP domain (Extended Data Figs. 4a,b). The

118 bottom layer is composed of the cytosolic N-terminal ankyrin repeat domain (ARD; comprising
119 six ankyrin repeats, ARs) and a coupling domain (CD), including a helix-turn-helix motif (HTH_{CD})
120 and β-sheets (β_{CD}), and a C-terminal domain (CTD) (Extended Data Fig. 4a). RhoA acts as an
121 auxiliary subunit, interacting with the ARD through three loops connecting AR2-AR3, AR3-AR4,
122 AR4-AR5, and with the membrane bilayer through the prenylated C-terminal tail. The apparent
123 stoichiometry of RhoA and each TRPV4 subunit is 1:1 based on the C1 reconstruction (Extended
124 Data Fig. 1b). The human tetrameric TRPV4-RhoA signaling complex structure exhibits a
125 canonical domain-swap tetrameric arrangement where the VSLD of TRPV4 from one subunit
126 interacts with the pore domain from the neighboring subunit (Extended Data Figs. 4b-f). The fold
127 and quaternary structure of full-length human TRPV4 are in stark contrast with the published cryo-
128 EM structure of truncated frog TRPV4, whose pore domains are not swapped (Extended Data Fig.
129 4g)[27]. Because the domain-swapped architecture is the well-accepted architecture of the TRP
130 channel superfamily[28], our TRPV4-RhoA structures represent physiologically relevant
131 conformations.
132
133 **Agonist- and antagonist-dependent TRPV4 gating**
134 We identified strong and unambiguous EM densities corresponding to GSK279
135 (antagonist), GSK101 (agonist), and 4α-PDD (agonist) within the cavity between the VSLD and
136 the TRP domain (termed here the VSLD cavity; Figs. 1f, 2a). These compounds are stabilized
137 within the VSLD cavity by many aromatic and polar residues. Due to their higher TMD map
138 quality, we only included the GSK279-bound closed state and the GSK101-bound open state for
139 subsequent analyses of ligand binding and gating.
140 As the shared binding region for GSK279 and GSK101 complicates functional studies of
141 TRPV4, we utilized the double mutant N456H/W737R (referred to as $TRPV4^{DM}$)[29] that can be

activated by 2-aminoethoxydiphenyl borate (2-APB) (Figs. 2b-e). The putative 2-APB binding site in TRPV4 is located at a distance from the VSLD cavity[30], thus 2-APB binding to $TRPV4^{DM}$ does not interfere with either GSK279 or GSK101 binding. Y553A, D743A, and F524A mutations on the background of $TRPV4^{DM}$ suppress TRPV4 activation by GSK101 relative to that by 2-APB (Fig. 2c), while D743A and D546A attenuate channel inhibition by GSK279 (Fig. 2e). Previous studies have suggested that the S2-S3 loop, S3, and S4 are involved in TRPV4 sensitivity to 4α–PDD and the inhibitor, HC067047[31,32], which is consistent with our findings (Extended Data Fig. 5a).

How is it that GSK279 and GSK101 impose opposite effects on TRPV4 gating while binding to a common set of residues in the VSLD cavity? We observe that going from the GSK279-bound closed state to the GSK101-bound open state, the S2-S3 linker (M534-S548) undergoes a loop-to-helix transition, thereby altering the interaction network among the VSLD, TRP domain, and CD (Fig. 2f). In the closed state, D531 (S2), Q550 (S3), D546 (S2-S3), and R594 (C-terminal half of S4; S4b) form a charged H-bond relay within the VSLD, while D743, R746 (TRP domain) and Y439 (CD; HTH_{CD}) connect the TRP domain and the CD (Fig. 2g, left). These two separate interaction networks appear to be decoupled between the VSLD and the TRP/CD. In contrast, the rearrangement of the S2-S3 linker in the open state couples the VSLD to the TRP domain and the CD. First, the D531-Q550-D546-R594 interactions within the VSLD are broken. As a result, Q550 (S3) interacts with both the hydroxyl group of GSK101 and N528 (S2), while R594 (S4b) forms a new salt-bridge interaction with D743 (TRP domain), and D531 (S2) interacts with R746 (TRP domain) (Fig. 2g, right), resulting in the ~4 Å downward swing of the TRP domain and rearrangement of the CD (HTH_{CD}) (Figs 2f,g and Extended Data Figs. 5b,c). Therefore, the opposing actions of agonist/antagonist binding to the same cavity in TRPV4 originate from the coupling or decoupling of the VSLD-TRP-CD subdomains mediated by ligand binding (Fig. 2g).

166 These conformational changes associated with channel activation propagate from the
167 ligand-binding site to the pore domain. The S4-S5 linker, S5, and PH rotate toward the central ion
168 conduction pathway, and S6 undergoes changes in the π-helix position (from M718 to V708) and
169 rotation at the C-terminus (C-terminal half of S6 [S6b]; residues N712-G719) (Extended Data Fig.
170 5b).
171

172 **Pore conformation changes during TRPV4 gating**

173 We observe extensive conformational changes in the TRPV4 pore domain during ligand-
174 dependent gating. The GSK279-bound closed state adopts a wide-set SF (I678-G679-M680) and
175 the narrowest constriction point of the S6 gate is at M718 (Figs. 3a-c). The diagonal distance
176 between G679 backbone carbonyls in the SF (12.2 Å) is too far to coordinate cations, while that
177 between the M718 sidechains (4.9 Å) is too narrow for ion conduction. However, in the GSK101-
178 bound open state, the SF and the PHs move closer to enable cation coordination (the diagonal
179 distance of G679 backbone carbonyl is 7.0 Å), which is consistent with previous mutagenesis
180 studies[33]. Meanwhile the pore-lining S6 helices rotate ~90°, thus changing the gate position (from
181 M718 to I715) and the gate opening (the diagonal distance at I715 is 8.4 Å) (Figs. 3c,d). This S6
182 rotation between the two states is due to the shift of the π-helix position on S6 (Fig. 3a), resulting
183 in a local secondary structure conversion between α- and π-helix along S6b, which is unique
184 amongst the TRP channels[34]. The conformational changes of S6 are facilitated by rearrangement
185 in the interfacial contacts with the neighboring S4-S5 linker (Extended Data Fig. 5d).

186 Interestingly, when compared to the closed state, we found that the pore cavity volume is
187 reduced, and the surface electrostatic potential becomes substantially more negative in the open
188 state (Fig. 3e). This was not observed in other TRPV channels[28]. Taken together, we posit that

189 these unusual changes in the pore help form the ion permeation path, similar to the canonical
190 tetrameric cation channel[28].

191 To validate the S6 gate position observed in the open-state structure, we performed Cd^{2+}-
192 dependent blocking of TRPV4. Extracellular application of Cd^{2+} does not affect the opening of
193 WT TRPV4 by GSK101 (Fig. 3f). Among cysteine mutants near the S6 gate (I715C, A716C,
194 L717C, and M718C), only I715C showed substantial inhibition of GSK101-elicited current by
195 extracellular Cd^{2+}, supporting the observation that I715 faces the ion permeation pathway in the
196 TRPV4 open state (Fig. 3f).

197

198 **Neuropathy mutations disrupt RhoA binding to TRPV4**

199 At the core of the small GTPase RhoA is a highly conserved G domain comprising a six-
200 stranded β-sheet (β1-β6), six helices (α1-α6), and a C-terminal variable region (Fig. 4a and
201 Extended Data Fig. 6). Switch I and II regions within the G domain adopt distinct GDP- or GTP-
202 dependent conformations, where the latter favors effector protein binding[35].

203 We performed focused-refinement on the RhoA and ARD region in the 3D reconstructions
204 of the GSK279-bound, apo, and GSK101-bound data. Although the EM density for the ARDs in
205 all three states exhibited high quality, that for RhoA was most well resolved in the GSK279-bound
206 closed state, which we used to unambiguously model RhoA and map its interaction with TRPV4
207 (Extended Data Figs. 2, 3a, and 3b). We resolved GDP within the RhoA-TRPV4 signaling
208 complex in the GSK279-bound closed state, and by including GTPγS before freezing grids we
209 observed density consistent with GTPγS in the open state (Extended Data Figs. 7a,b). We did not,
210 however, observe substantial structural differences of RhoA between the GDP- and GTPγS-bound
211 forms in complex with the closed- and open-states of TRPV4, respectively (Extended Data Fig.
212 7c). We used the model from the GSK279-bound closed state for our analysis of RhoA-TRPV4

213 interactions. Notably, while the switch I in RhoA resembles the GDP-bound RhoA structure, the
214 switch II is distinct from either the GDP- or the GTP-bound RhoA structure (PDB IFTN and 1A2B;
215 Extended Data Fig. 7d). The interfacial contact that associates TRPV4 and RhoA is mediated
216 principally by electrostatic interactions between β1 and β3, switch I, and switch II in RhoA and
217 AR2-AR5 in TRPV4 (Fig. 4a and Extended Data Fig. 7e). Sequence comparisons indicate that the
218 interfacial residues are unique to the TRPV4 ARD across all TRPV channels, and to Rho isoforms
219 amongst other small GTPases, suggesting that the observed RhoA binding mode is specific to
220 TRPV4 (Fig. 6)[22].

221 Strikingly, most residues mutated in TRPV4-mediated neuropathy (R237, R269, R315, and
222 R316) are clustered at the interface with RhoA (Fig. 4a). R232, a reported TRPV4-neuropathy
223 mutation site, does not directly participate in the interfacial contact but does form an intra-subunit
224 salt-bridge with another neuropathy-causing residue E183, which is likely important for tuning
225 electrostatics and the local conformation of the RhoA-binding surface of the ARD (Extended Data
226 Fig. 7f). Therefore, disease-causing mutations in TRPV4 likely weaken the interactions with
227 RhoA[22]. Notably, we also found that several cancer-related mutation sites in RhoA, such as A3,
228 R5, and E50[36-38], are located at the interface with the TRPV4 ARD (Figs. 4b,c), providing evidence
229 for an interplay between TRPV4 and RhoA in cancer[5,21,39], although these RhoA mutations may
230 also impact effector binding more broadly.

231 To probe the interactions between TRPV4 and RhoA, we first performed co-
232 immunoprecipitation of GFP-tagged WT or mutant TRPV4 with Myc-tagged WT or mutant RhoA
233 overexpressed in HEK293T cells[22]. We previously showed that neuropathy-causing mutations
234 (R232C, R237L, R269C, R315W) in TRPV4 disrupt the interaction with RhoA, consistent with
235 our structures (Figs. 4b,c). We further mutated residues in RhoA (R5, E54, D76) and TRPV4 (E183
236 and D263) that form the RhoA-TRPV4 interface. All mutants tested ($R5E^{RhoA}$, $E54H/L/K^{RhoA}$,

237 D76A/L/K/R^{RhoA}, E183A/C/K^{TRPV4}, and D263A/L/K/N^{TRPV4}) substantially decreased the amount
238 of immunoprecipitated partner proteins (TRPV4 and RhoA) (Fig. 4d). We then tested the effects
239 of these mutations on TRPV4 function using ratiometric calcium imaging. When we tested TRPV4
240 mutant function, we opted not to overexpress RhoA but rather to rely on interaction with
241 endogenous RhoA. Compared to WT TRPV4, E183A/C/K or D263A/L/K/N mutations result in
242 increased basal and hypotonic saline-induced calcium influxes, similar to the neuropathy mutant
243 R269C mutation[22]. We then tested the effect of RhoA mutations on TRPV4 channel activity, in
244 experiments in which we overexpressed both TRPV4 and RhoA. Whereas expression of WT RhoA
245 strongly suppressed both basal and hypotonic saline induced Ca^{2+} influx (Figs. 1b and 4d), RhoA
246 mutants demonstrated reduced suppression of TRPV4 channel activity (Fig. 4d). Importantly, the
247 degree of suppression of TRPV4 activity correlated with the interaction strength between the RhoA
248 mutants and TRPV4 (Fig. 4d). These data demonstrate that TRPV4-RhoA interaction strength
249 strongly correlates with TRPV4 channel activity, and that disruption of this interaction underlies
250 the gain of function due to neuropathy mutations within the ARD. This suggests that balancing the
251 two different neurophysiological signaling pathways (calcium signaling and actin cytoskeleton
252 remodeling) requires fine tuning of the TRPV4-RhoA interaction.
253

254 **RhoA-dependent TRPV4 gating**

255 Despite only subtle conformational changes in RhoA, the buried surface area between
256 RhoA and TRPV4 in the open state is reduced (~684 Å^2) compared to that observed in the closed
257 state structure (~752 Å^2), suggesting RhoA-TRPV4 interactions become weaker in the open state
258 (Extended Data Fig. 7g). To compare the relative occupancy and/or dynamics of RhoA bound to
259 TRPV4 in different channel functional states, we lowpass filtered the cryo-EM maps of the closed,
260 apo, and open state structure at the same resolution (4 Å) and applied the same value of B-factor

261 sharpening. Notably, the EM density for RhoA progressively decreases from the closed to the apo
262 then to the open states, suggesting that the occupancy decreases and/or bound RhoA becomes more
263 flexible during TRPV4 gating (Fig. 5b). Consistent with this observation, further cryo-EM 3D
264 classifications of the closed and the open state reconstructions show that the closed state
265 reconstruction contains a major class with strong RhoA density while the open state reconstruction
266 contains classes with weak RhoA density (Extended Data Fig. 9). The apparent differential
267 resolution of RhoA density between the closed, apo, and open states led us to hypothesize the state-
268 dependent RhoA binding affinity to TRPV4.

269 TRPV channels are highly allosterically coupled across their domains, as was previously
270 shown[40], and because we observed progressive changes in RhoA occupancy during gating we
271 attempted to infer the effect of RhoA on TRPV4 gating. Structural alignment at the TMDs show
272 that each ankyrin repeat (AR) in the ARD swings toward the membrane by ~6 Å from the closed
273 to the open state (Fig. 5d). When viewed from the cytoplasmic side, individual ARs rotate
274 clockwise in addition to the upward swing of the ARD, rather than a concerted rotation of the
275 tetrameric ARD ring (Fig. 5c). Movements in the ARD propagate as conformational changes in
276 the CD (HTH_{CD}), and in turn the TRP domain and the VSLD (Fig. 5e), as essential gating steps in
277 TRPV4 activation (Fig. 2). RhoA, which is anchored to the membrane bilayer via its prenylated
278 C-terminus and binds to TRPV4 at the cytoplasmic ARD, exerts forces on the ARD analogous to
279 a clamp, which suppresses ARD motion and thus TRPV4 activation (Fig. 5f).

280

281 **Discussion**

282 Here we resolve, for the first time, human TRPV4 structures in complex with the small
283 GTPase RhoA and elucidate structural mechanisms underlying the crosstalk between RhoA and
284 TRPV4. The rigid-body rotation of the ARD domain couples the CD, the TRP domain, and VSLD,

285 leading to TRPV4 opening (Figs. 2g and 5e). Through membrane-anchored RhoA
286 binding/dissociation, Nature has designed a means to control the ARD rearrangement and therefore
287 TRPV4 gating. Although our current studies focus on the effect of RhoA on TRPV4 function,
288 conversely, TRPV4 activity can modulate RhoA unbinding and release[22]. Once TRPV4 is
289 activated, the membrane-bound RhoA is released to regulate cytoskeleton dynamics upon
290 activation by TRPV4-mediated calcium influx[41].

291 While the localization of neuropathy-associated TRPV4 mutations at the TRPV4-RhoA
292 interface suggests that control of this signaling complex is particularly important in the nervous
293 system, TRPV4-RhoA interactions are likely to play a fundamental role in signaling in other
294 disease states. Intriguingly, we demonstrated that several cancer-related mutations of RhoA also
295 disrupt the TRPV4-RhoA binding interface. Although these mutations may interrupt RhoA
296 binding with several partners, these data are consistent with prior work demonstrating a role for
297 TRPV4-RhoA in the metastatic cascade and tumor vascularization[5,21,39]. TRPV4-RhoA
298 interactions are also likely essential in endothelial (e.g. lung, retinal, intestinal) and epithelial (e.g.
299 skin, lung) cells, where both proteins have been shown to play key roles in barrier maintenance
300 [21,39,42]. Importantly, numerous studies have reported that RhoA and other small GTPases can affect
301 the function of various ion channels, including K^+ channels, several other TRP channels, epithelial
302 Na^+ channels, and acid-sensing ion channels[12-16]. Further work will be needed to determine
303 whether these other functional channel-GTPase couplings involve direct interactions, and if so,
304 whether similar or distinct structural mechanisms are utilized to those described here.

305 TRPV4 is a well-established osmosensor[18] and is also reported to respond to shear stress,
306 but the structural mechanisms mediating channel activation by these stimuli have not been
307 determined. Osmosensors can sense either the direct change in the extracellular water activity or
308 subsequent modifications in cellular organization[43]. We speculate that the wide-set pore domain

309 in the closed state of TRPV4 and its unusual pore conformational changes upon channel activation
310 contribute to channel sensitivity to changes in extracellular fluid activity or shear stress. Moreover,
311 the direct association with plasma membrane-anchored RhoA may enable TRPV4 to detect
312 changes in cellular shape and morphology induced by osmotic shock or mechanical force.
313 Consistent with this speculation, RhoA is activated under cell stretch[44], and the interaction of
314 TRPV4 with actin is essential for cell-swelling-induced channel activation[45].

315 Our studies also deciphered mechanisms of ligand-dependent TRPV4 activation and
316 inhibition. The binding of antagonists and agonists to a shared site within the VSLD cavity leads
317 to opposing conformational changes on the TRPV4 pore. Our structural analysis elucidated that
318 agonist binding couples, whereas antagonist binding decouples, the interaction network amongst
319 the VSLD, the TRP domain, and the CD. Our discoveries of the human TRPV4 structure bound to
320 the clinical candidate antagonist GSK279, as well as the molecular mechanisms of ligand-
321 dependent TRPV4 gating will facilitate the development of drugs targeting TRPV4. For example,
322 with this structure, one can modify GSK279 or find compounds with new scaffolds (via virtual
323 screening) to increase their potency or efficacy. Furthermore, the presented structures delineate
324 principles of channel inhibition that can be utilized for virtual screening for compounds that could
325 bind TRPV4 at different locations but exert similar inhibitory decoupling effects.
326
327
328
329
330
331
332

333 **Table 1. Cryo-EM data collection, refinement, and validation statistics.**

	hTRPV4-RhoA GSK2798745 (EMDB-28975) (PDB-8FC7)	hTRPV4 GSK1016790A (EMDB-28976) (PDB-8FC8)	hTRPV4-RhoA GSK1016790A (PDB-8FCB)	hTRPV4-RhoA apo (EMDB-28977) (PDB-8FC9)	hTRPV4 4α-PDD (EMDB-28978) (PDB-8FCA)
Data collection and processing					
Magnification	81,000	81,000		81,000	81,000
Voltage (kV)	300	300		300	300
Electron exposure (e^-/Å^2)	60	60		60	60
Defocus range (μm)	-0.8 to -1.8	-0.8 to -1.8		-0.8 to -1.8	-0.8 to -1.8
Pixel size (Å)	1.08	1.08		1.08	1.08
Symmetry imposed	C4	C4		C4	C4
Initial particles images (no.)	2,111,563	8,119,132		3,412,804	4,418,471
Final particles images (no.)	119,462	207,645		172,225	375,644
Map resolution (Å)	3.3	3.47		3.75	3.41
FSC threshold	0.143	0.143		0.143	0.143
Refinement					
Initial model used (PDB code)	TRPV1 (7LP9) RhoA (1FTN)	PDB-8FC7		PDB-8FC7	PDB-8FC7
Map sharpening *B* factor (Å^2)	-136	-183		-195	-140
Model composition					
Non-hydrogen atoms	25,716	19,764	25,968	21,812	18,224
Protein residues	3,284	2,468	3,228	3,092	2,352
Ligands	12	8	12	0	4
B factors(Å^2)					
Protein	90.02	81.88	101.36	136.85	61.33
Ligand	83.5	46.42	68.17	-	96.78
R.m.s deviations					
Bond lengths (Å)	0.004	0.004	0.004	0.004	0.005
Bond angles (°)	0.919	0.945	1.134	0.562	0.968
Validation					
MolProbity score	1.56	1.22	1.35	1.06	1.22
Clashscore	5.17	4.06	4.48	3.81	4.12
Poor rotamers (%)	0	0.19	0.16	0.22	0
Ramachandran plot					
Favored (%)	95.83	97.88	97.38	98.56	97.59
Allowed (%)	4.17	2.12	2.62	1.44	2.41
Disallowed (%)	0	0	0	0	0

334

335

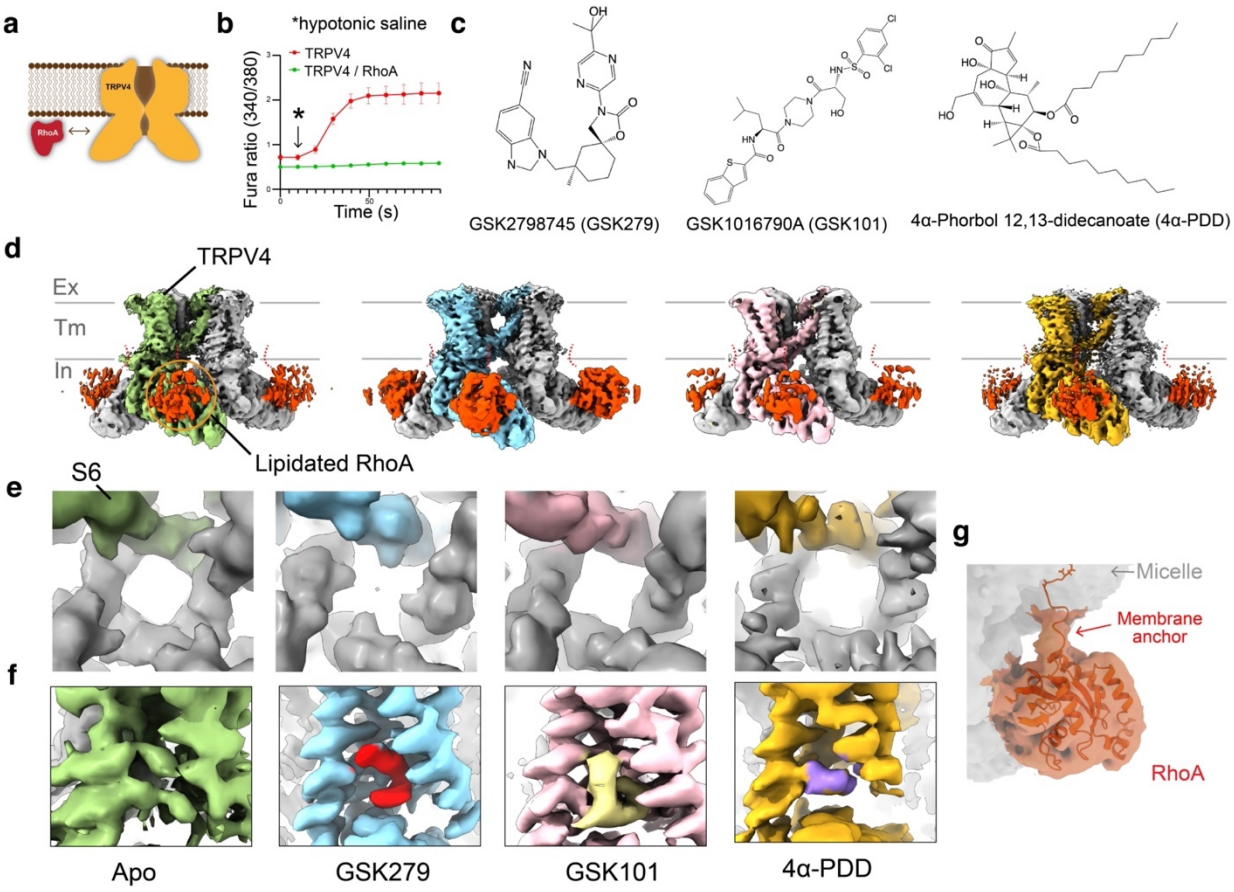

Fig. 1. Functional characterization and structure determination of the human TRPV4 – RhoA complex

a, Schematic drawing of the functional TRPV4-RhoA interaction.

b, Averaged calcium imaging traces before and after hypotonic stimulation, denoted by the arrow. Expression of WT TRPV4 alone causes elevated baseline and stimulated calcium influx relative to the co-expression of TRPV4 WT and RhoA. Data are presented as means ± SEM.

c, Chemical structures of GSK1016790A (GSK101), GSK2798745 (GSK279), and 4α-Phorbol 12,13-didecanoate (4α-PDD).

d, Cryo-EM structures of hTRPV4-RhoA complex in the apo, closed, open, and 4α-PDD-open states, as indicated. Thresholding, 0.24 (green), 0.25 (cyan), 0.25 (pink), 0.26 (gold)

e, Close-up view at the S6 gate of 3D reconstructions from (**d**) viewed from the intracellular side, at thresholding 0.14, 0.25, 0.26, and 0.185, respectively.

f, Close-up view at the ligand binding site of 3D reconstructions from (**d**) at thresholding 0.23, 0.36, 0.34, and 0.22, respectively.

351 **g**, Cryo-EM density of RhoA and lipidated tail of GSK279-hTRPV4-RhoA, viewed from the
352 intracellular side, at thresholding 0.09.
353
354

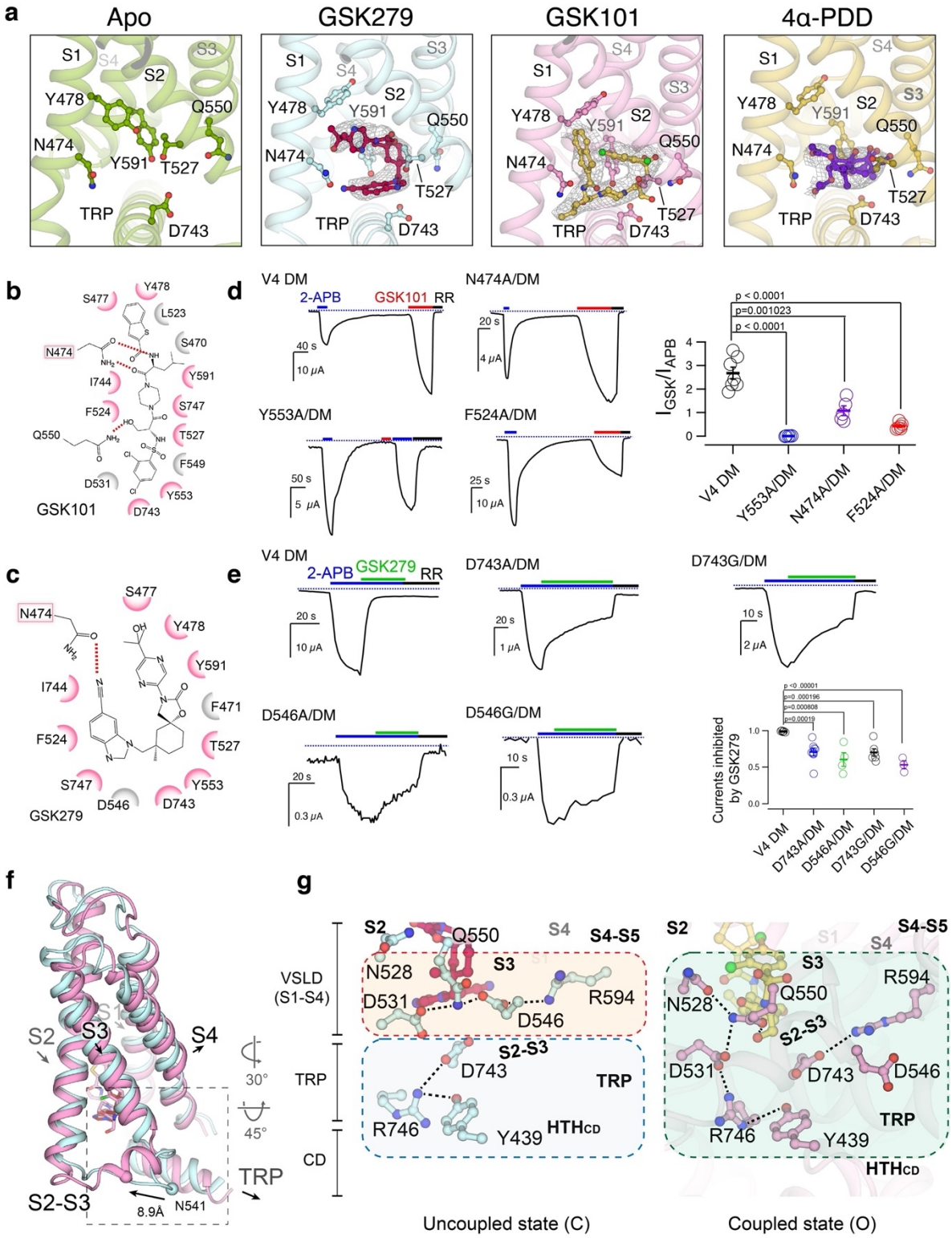

Fig. 2. Antagonist- and agonist-binding in the hTRPV4 channel

357 **a**, Cryo-EM densities (gray mesh) for ligands (GSK279; red stick, GSK101; gold stick, and 4α–
358 PDD; violet stick) in apo, closed, open, and 4α–PDD-open. Densities are contoured at 0.23, 0.36,
359 0.34, and 0.22 thresholding, respectively. Sidechains of residues are shown in sticks.
360 **b**,**c**, Ligplot schematics of GSK279–TRPV4 and GSK101-TRPV4 interactions, where residues
361 within 3.8 Å to the ligands are shown. Pink colored residues are shared at both interactions.
362 **d**, Probing the agonist binding site. Representative two-electrode voltage clamp (TEVC) recording
363 of human TRPV4 mutant (hTRPV4 DM) and additional mutants made with the background
364 hTRPV4 DM as indicated in the figure. The currents were elicited by 2 mM 2-APB and 5 μM
365 GSK101 as denoted by colored horizontal lines. Voltage was held at -60 mV then ramped to +60
366 mV over 300 ms every 2 seconds. Plotted here are the currents at -60 mV. The dotted line indicates
367 zero-current level. Right panel: Summary of current responses to 5 μM GSK101 relative to
368 saturating 2-APB (2 mM) at room temperature. Values for individual oocytes are shown as open
369 circles with mean ± S.E.M. shown (n = 5–7). P values are calculated by two-tailed Student's t test.
370 **e**, Probing the inhibitor binding site. TEVC recordings of hTRPV4 DM (N456H/W737R) and
371 additional mutants made in the background of hTRPV4 DM, as indicated. Currents at -60 mV
372 induced by 2 mM 2-APB then co-application of 4 μM GSK279 followed by 20 μM ruthenium red,
373 as indicated by colored horizontal lines, using the same voltage protocol as in (**c**). Summary of
374 current inhibition by 4 μM GSK279 relative to current from saturating 2-APB (2 mM) at room
375 temperature. Values for individual oocytes are shown as open circles with mean ± S.E.M. shown
376 (n = 3–9). P values are calculated by two-tailed Student's t test.
377 **f**, Comparison of conformational changes in the VSLD of GSK279-hTRPV4-RhoA (cyan) and
378 GSK101-hTRPV4-RhoA (pink). Ligands are shown as sticks. Arrows indicate helix movements
379 and rotations.
380 **g**, Comparison of coupling networks at the VSLD, CD and TRP domain in closed and open states.
381 Dashed lines indicate hydrogen bonds and salt-bridges.
382
383
384
385
386

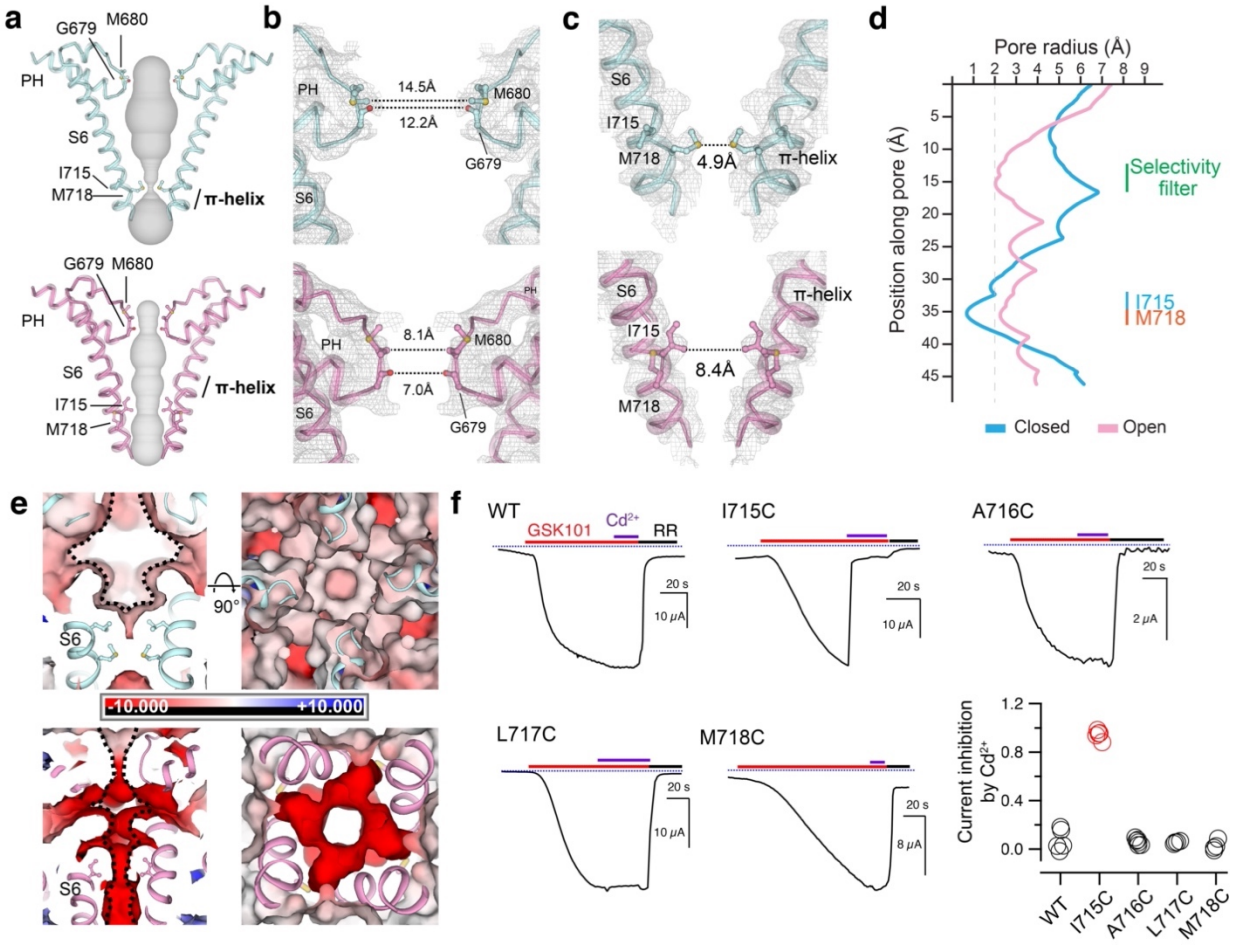

Fig. 3. Structural changes in the S6 gate and SF position during channel gating

a, Ion permeation pathway in the closed and open state shown as gray surfaces. S6 helices from two protomers are shown in cartoon. Only two subunits are shown for clarity. Gating and selectivity filter residues shown as sticks.

b,**c**, Close-up views of the SF region (**b**) and S6 gate (**c**) for the closed and open states. The dotted lines indicate diagonal distances between gating residues of opposite protomers. Gray mesh indicates cryo-EM densities contoured at 0.3 (top) and 0.4 (bottom) thresholding, respectively.

d, Pore radii calculated using the HOLE program in Coot for representative TRPV4 structures as color-coded. The minimal radius for a hydrophobic gate to be open is considered 2.0 Å. Residues corresponding to the SF (M680 and G679) and the S6 gate (I715 and M718) are denoted.

e, APBS surface electrostatics of the pore in the closed and open states as viewed from the membrane plane (right) and from the extracellular side (left). S6 helices and SF region are shown in cartoon and gating residues as sticks.

401 **f**, Representative time-course recording of hTRPV4 WT and mutants. Currents elicited by 5 μM
402 GSK101 and co-application with 10 μM Cd^{2+} followed by 20 μM ruthenium red (RR) as indicated
403 by colored horizontal lines. The voltage was ramped from -60 mV to +60 mV in 300 ms every 2
404 seconds. The currents at -60 mV were used for the plot. Dotted blue lines indicate zero-current
405 level. Right panel, summary of current inhibition by 10 μM Cd^{2+} relative to 5 μM GSK101 induced
406 currents. Values for individual oocytes are shown as open circles (n = 4–7).
407
408
409
410
411
412
413
414
415
416
417
418
419
420
421
422
423
424
425
426

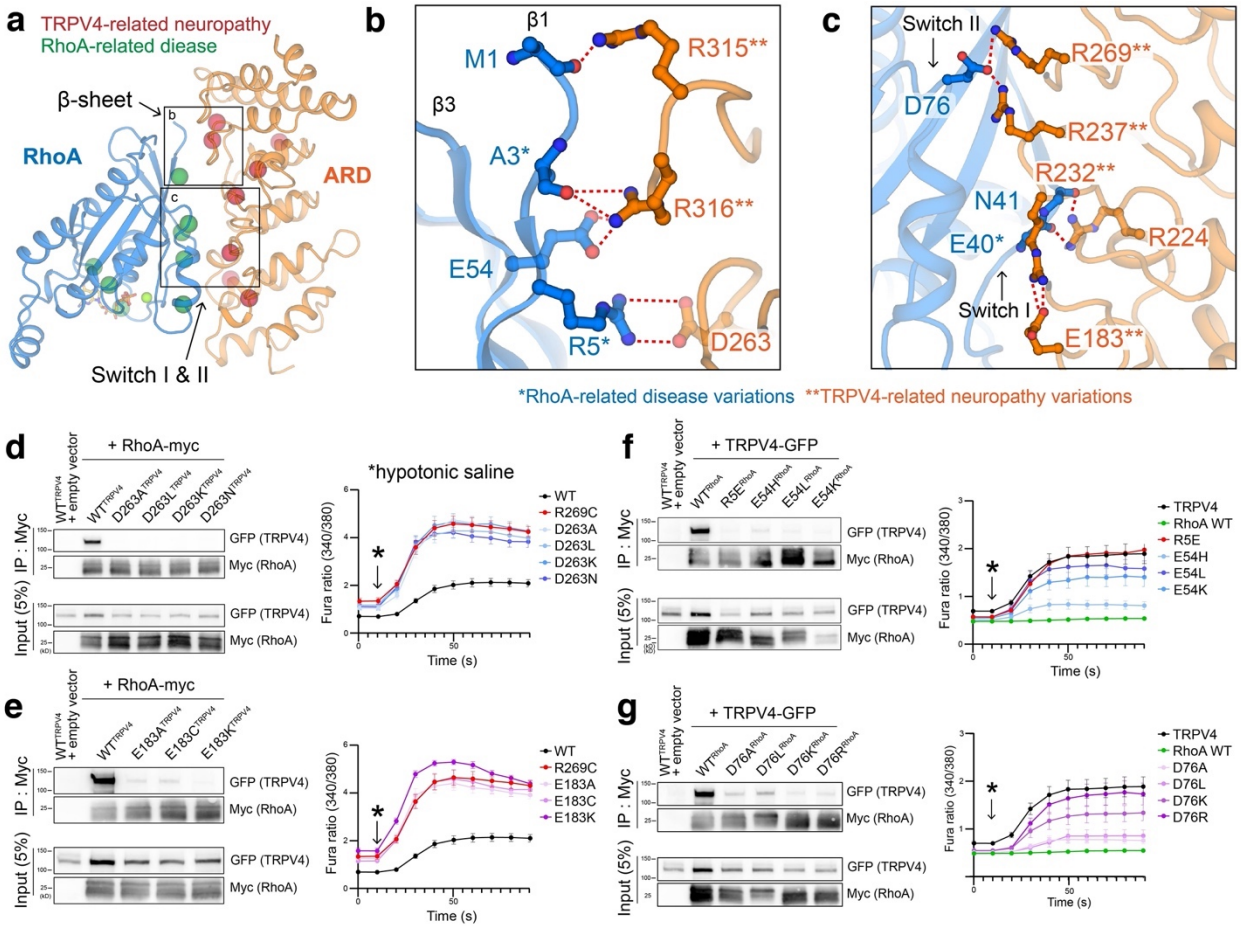

Fig. 4. Interaction between hTRPV4 ARD and RhoA

a, Overall interaction interface of hTRPV4 ARD and RhoA. Disease-causing mutations mapped onto the TRPV4-RhoA interface. Mutations causing peripheral neuropathy of TRPV4- and RhoA-related diseases are shown as red and green spheres, respectively.

b,**c**, Detailed hTRPV4 ARD – RhoA interactions within the β1-β3 region (**b**) and switch region (**c**). RhoA residues are colored blue, TRPV4 residues are colored orange. * disease-causing mutations in RhoA and ** neuropathy-causing mutations in TRPV4. The red dashed lines indicate salt-bridge interactions.

d-g, (Left panels) Co-immunoprecipitation of HEK293T cells transfected with TRPV4-GFP (**d**, E183A/C/K; **e**, D263A/L/K/N) and RhoA-Myc (**f**, R5E, E54L/H/K; **g**, D76A/L/K/R) demonstrates that mutations at the TRPV4-RhoA interface reduces their interaction. (Right panels) Representative plots from ratiometric calcium imaging experiments. MN-1 cells were transfected with GFP-tagged TRPV4 plasmids only (**d** and **e**) and GFP-tagged TRPV4 and RhoA plasmids (**f**

441 and **g**) and loaded with Fura-2 AM calcium indicator. Baseline and hypotonic-stimulated calcium
442 responses were then measured over time.
443
444
445
446
447
448
449
450
451
452
453
454
455
456
457
458
459
460
461
462
463
464
465

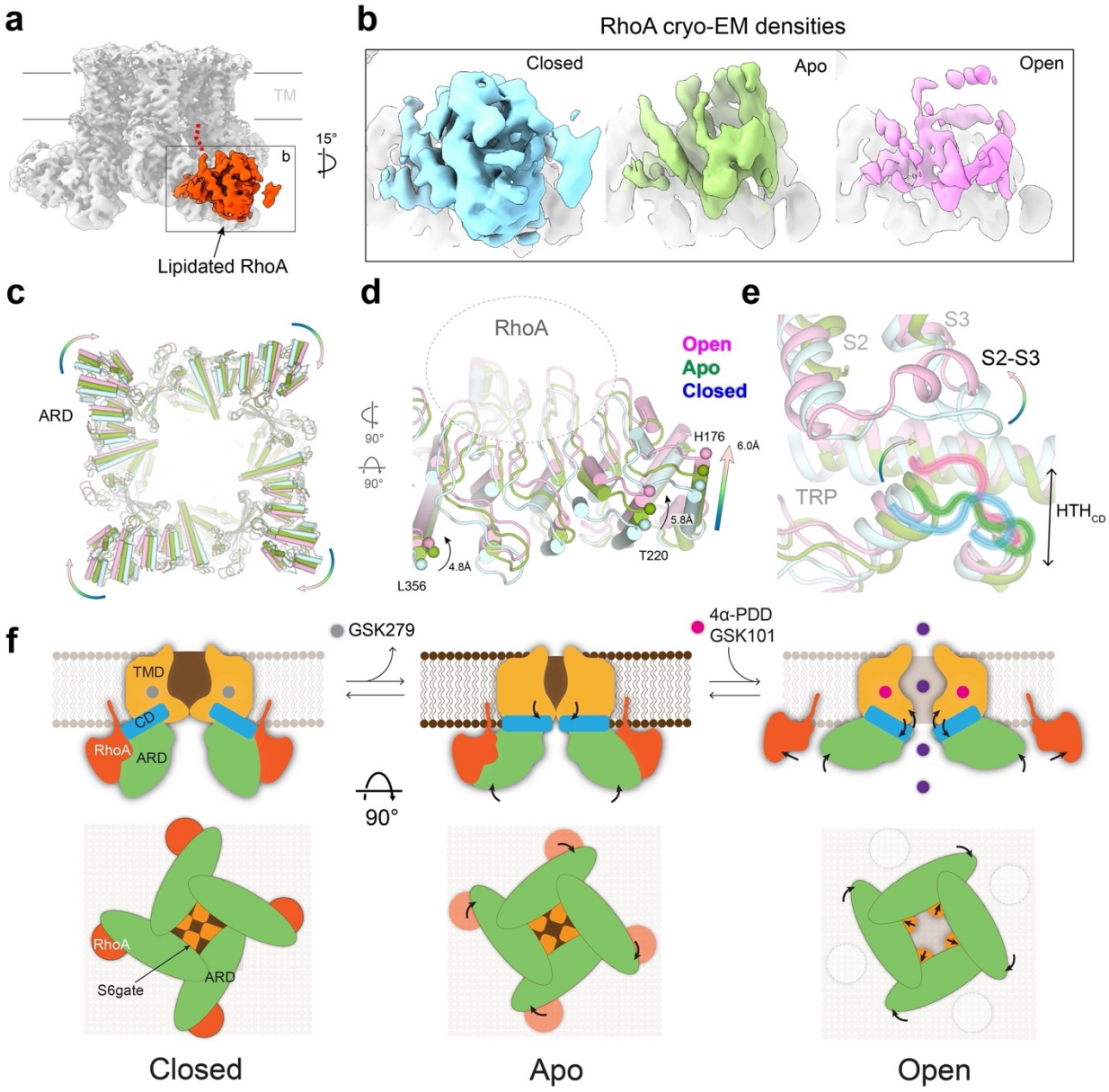

Fig. 5. Structural basis of RhoA-dependent gating of hTRPV4

a, Cryo-EM reconstruction of GSK279-hTRPV4-RhoA, with the RhoA from one protomer highlighted in red at thresholding 0.29.

b, Side-by-side comparison of cryo-EM densities of RhoA in closed (cyan), apo (green), and open (pink) states at thresholding 0.25.

c-e, Comparison of closed, apo, and open structures viewed from the intracellular side (**c**). Close-up view of the ARD (**d**). and coupling domain (**e**; HTH_{CD}, TRP, and S2-S3). Arrows indicate movements of the ARD. ARD/CD movement occurs at an individual protomer level.

f, Ligand-dependent channel gating of hTRPV4–RhoA. Schematic illustration of the conformational rearrangements in the S6 gate, ARD, and RhoA during TRPV4 gating.

507 **Materials and Methods**

508 Protein expression and purification

509 The *Homo sapiens* full-length TRPV4 (hTRPV4) was cloned into a modified pEG
510 BacMam vector[46] in frame with a FLAG-tag and 10×His-tag at the C terminus. The hTRPV4-
511 RhoA complex was expressed by baculovirus-mediated transduction of the human embryonic
512 kidney (HEK) GnTI^{-} suspension cells, cultured in FreeStyle 293 medium (Life Technologies) with
513 2% (vol/vol) FBS at 8% CO_2. hTRPV4 baculovirus was generated following the Bac-to-Bac®
514 Baculovirus Expression System protocol (Life Technologies). Cultures were infected at a cell
515 density of ~1.5M mL^{-1} with 1.5 – 2 % (v/v) P3 or P4 baculovirus for hTRPV4. After 18 h of
516 shaking incubation at 37 °C, 10 mM sodium butyrate was added, and the growth temperature was
517 lowered to 30 °C to boost protein expression. After 68-72 h, the cells were harvested by
518 centrifugation at 550 xg and resuspended in lysis buffer (20 mM Tris pH 8, 150 mM NaCl, 12 µg
519 ml^{-1} leupeptin, 12 µg ml^{-1} pepstatin, 12 µg ml^{-1} aprotinin, 2 µg ml^{-1} Dnase I, 1 mM PMSF, 10%
520 (v/v) glycerol, 1 mM dithiothreitol (DTT), 1% (w/v) Lauryl Maltose Neopentyl Glycol (LMNG;
521 Anatrace), and 0.1% (w/v) cholesteryl hemisuccinate (CHS; Anatrace). Membranes were
522 solubilized at 4 °C by gentle agitation for 2 h followed by centrifugation at 8,000xg for 30 min to
523 remove insoluble material. The supernatant was subsequently incubated with anti-FLAG M2 resin
524 (Sigma-Aldrich) for 40 min at 4 °C with gentle agitation. The resin was then packed onto a gravity-
525 flow column (Bio-Rad) and washed with 10 column volumes (CV) of high salt wash buffer (20
526 mM Tris pH 8.0, 150 mM NaCl, 0.1% LMNG, 0.01% CHS, 5mM ATP, 1 mM DTT, and 5%
527 glycerol) followed by 10 CV of low salt wash buffer 1 (20 mM Tris pH 8.0, 500 mM NaCl, 0.1%
528 LMNG, 0.01% CHS, 1 mM DTT, and 5% glycerol) , and then 10 CV of low salt wash buffer 2
529 (20 mM Tris pH 8.0, 150 mM NaCl, 0.03% LMNG 0.003% CHS, 1mM DTT and 5% glycerol).
530 The hTRPV4-RhoA complex was eluted by 5CV of elution buffer (20 mM Tris pH 8.0, 150 mM
531 NaCl, 0.03% LMNG, 0.003% CHS, 1 mM DTT, 5% glycerol, 0.150 mg mL^{-1} FLAG peptide). The
532 eluted protein complex was concentrated and further purified by size exclusion chromatography
533 (SEC) on a Superose 6 Increase column (Cytiva Life Science) equilibrated with SEC buffer (20
534 mM Tris pH 8.0, 150 mM NaCl, 0.00075% LMNG, 0.000075% CHS, 0.0003% glycol-diosgenin
535 (GDN; Anatrace), 1 mM DTT, and 5% glycerol).

536

537 Cryo-EM sample preparation and data acquisition

538 hTRPV4-RhoA peak fractions from SEC were concentrated to 0.8 – 1.2 mg mL^{-1}. All
539 samples were incubated with different ligand conditions at 4 °C for 15-20 min prior to freezing
540 grids. For the apo-hTRPV4-RhoA sample, 2% (v/v) DMSO was added to the purified protein
541 instead of ligands. For the GSK279-hTRPV4-RhoA, sample was incubated with 20 μM
542 GSK2798745 (GSK279; Medchemexpress). For the GSK101-hTRPV4-RhoA, 20 μM
543 GSK1016790A (GSK101; Tocris) and 2 mM Guanosine 5'-[γ-thio] triphosphate (GTPγS; Sigma-
544 Aldrich) were incubated with the protein. For the 4α-PDD-hTRPV4-RhoA, sample was incubated
545 with 4α-Phorbol 12,13-didecanoate (4α-PDD; Sigma-Aldrich) and 2mM GTPγS. All grids were
546 prepared with a Leica EM GP2 plunge freezer (Leica) at 4 °C and 95% humidity. 3 μL of sample
547 was applied to a freshly glow-discharged UltrAuFoil R1.2/1.3 300 mesh grids (Quantifoil), blotted
548 for 1.5 – 2.0 s, depending on the specific ligand conditions, to obtain optimal ice thickness for data
549 collection.
550 Cryo-EM datasets for the apo-hTRPV4-RhoA, GSK279-hTRPV4-RhoA, GSK101-
551 hTRPV4-RhoA, and 4α-PDD-hTRPV4-RhoA were collected with Titan Krios microscope (FEI)
552 operating at 300 keV equipped with a K3 detector (Gatan) with GIF BioQuantum energy filter (20
553 eV slit width: Gatan) in counting mode, using the Latitude-S automated data acquisition program
554 (Gatan). Movie datasets were collected at a nominal magnification of 81,000x with a pixel size of
555 1.08 Å per $pixel^{-1}$ at specimen level. Each movie contained 60 frames over 4.6 s exposure time,
556 using a dose rate ~15 $e^{-}Å^{-2}s^{-1}$, resulting in the total dose of ~60 $e^{-}Å^{-2}$. The nominal defocus ranged
557 from -0.8 to −2.0 μm.
558
559 Cryo-EM data processing
560 A total of 5,666, 3,877, 17,040, and 8,226 movies were collected for the apo-hTRPV4-
561 RhoA, GSK279-hTRPV4-RhoA, GSK101-hTRPV4-RhoA, and 4α-PDD-hTRPV4-RhoA
562 structures, respectively. All four datasets were processed similarly, as illustrated in Extended Data
563 Fig. 1c with RELION 4.0[47] and cryoSPARC[48]. Beam-induced motion correction and dose-
564 weighting were performed using MotionCor2[49], followed by CTF estimation using Gctf[50] in
565 RELION. Micrographs were subsequentially selected based on astigmatism, CTF fit quality, CTF
566 estimated maximum resolution, and defocus values. An initial set of particles were manually
567 picked and subjected to a reference-free 2D classification (k = 7, T = 2), from which the best two
568 to three classes were selected as reference for a templated-based auto-picking in RELION.
569 Particles were re-centered, and re-extracted Fourier binned 4x4 (64-pixel box size) and imported

570 to cryoSPARC. Two rounds of 2D classification with 50 classes were used to remove
571 contamination and false noise picks, like chaperones and junk particles. The particles were
572 imported to RELION and subjected to reference-free 2D classification (k = 50, T = 2), ignoring
573 the CTFs until the first peak option. Classes were selected that showed apparent structure features
574 of the hTRPV4-RhoA complex. These particles were subsequently subjected to 3D classification
575 (k=3 or 4, T=8) with C1 symmetry with image alignment using a previously published TRPV1
576 map (EMD-23473, low-passed filtered to 60 Å) as a reference without masking. The class showing
577 the apparent shape of the hTRPV4-RhoA complex was selected, re-centered, and re-extracted
578 Fourier binned 2x2 for further classification. Refined particles at 2x2 Fourier binning were
579 subjected to 3D classification with image alignment (K=3, T=8) and C1 symmetry. The class
580 showing substantial densities for transmembrane helices and RhoA, was selected, re-centered, re-
581 extracted without binning, and subjected to 3D classification without image alignment (k=2 or 3,
582 T= 8-12) with a soft mask covering TRPV4 and RhoA with C4 symmetry imposed. The particles
583 from the class with the best-resolved transmembrane helices were subjected to 3D- auto-
584 refinement with a soft TRPV4-RhoA mask. The refined particles were processed for CTF
585 refinement,[51] Bayesian polishing[52] then subjected to particle subtraction to resolve the strong
586 density at the transmembrane domains (TMDs), followed by focused 3D classification. The tight
587 mask for signal subtraction was made by subtracting out all unnecessary signals from the previous
588 consensus 3D reconstruction, including detergent micelle, parts of the cytosolic domains, and
589 RhoA. The subtracted particles by the tight mask were subjected to focused-3D classification
590 without image alignment (k = 2, T =16 or 20). Particles comprising the best-featured class at TMDs
591 were reverted to original particles, which were input to 3D auto-refinement with a hTRPV4-RhoA
592 full mask. Additional CTF refinement and Bayesian polishing were performed to improve the
593 overall map quality. Finally, particles yielding the best 3D reconstruction from RELION were
594 imported into cyroSPARC and subjected to non-uniform (NU) refinement[53] with a full mask. To
595 improve the EM density quality at the TMDs of TRPV4 the particles were subjected to particle
596 subtraction of the four RhoA densities, followed by NU refinement. In order to resolve the
597 unambiguous EM density around RhoA for GSK279-hTRPV4-RhoA and GSK101-hTRPV4-
598 RhoA structures, we performed local refinement at the level of one monomeric ARD and RhoA
599 by subtracting signals of the tetrameric TMDs, the other three ARDs, and RhoAs. A detailed data
600 processing flowchart for the GSK101-hTRPV4-RhoA structure is illustrated in Extended Data Fig.
601 2.

602 Model building, refinement, and validation

603 For manual model building in Coot[54], the published cryo-EM structure of *Rattus*
604 *norvegicus* TRPV1 (PDB: 7LP9) and published crystal structure of GDP-bound RhoA (PDB:
605 1FTN) were docked into the cryo-EM map for GSK279-hTRPV4-RhoA. The angle between the
606 ARD and TMD was first rigid body adjusted into the EM densities, separately. Secondary
607 structures were then rigid body fit into the EM densities using bulky aromatic residues to ensure
608 correct register assignment.

609 The focus refined TRPV4 channel map and ARD-RhoA focused map facilitated register
610 assignment at S4-S5, S6-TRP flexible linkers and RhoA (Extended Data Fig. 3). The placement
611 of individual residues was adjusted by rigid body fitting then manually refined using real space
612 refinement in Coot, with ideal geometric and secondary structure restraints. The GSK279-
613 hTRPV4-RhoA models served as the initial reference for model building of the GSK101-hTRPV4-
614 RhoA, apo-hTRPV4-RhoA, and 4α-PDD-hTRPV4-RhoA structures. The restraints for ligands and
615 lipid, including GSK279, GSK101, 4α-PDD, and CHS were generated from isomeric SMILES
616 strings using the eLBOW tool[55] in PHENIX to fix bond lengths and angles. The manually built
617 structure models with ligands were subjected to real-space refinement in PHENIX using cryo-EM
618 maps with global minimization, rigid body refinement and B-factor refinement[56] .
619 Problematic regions identified by the MolProbity server(http://molprobity.biochem.duke.edu)[57],
620 including geometry outliers and Ramachandran outliers, were manually adjusted in Coot. The FSC
621 curves for the model against the full map and both half-maps were generated by comprehensive
622 validation[58] in PHENIX. The FSCs were in good agreement with each other, indicating models
623 were not over-fitted and refined. Structural illustrations and analysis were performed in Coot[54],
624 PyMO[59], UCSF Chimera[60], and UCSF ChimeraX[61]. For the figure preparations of cryo-EM density
625 maps, UCSF ChimeraX and PyMOL were used.

626

627 Two-electrode voltage-clamp electrophysiology

628 The WT human TRPV4 DNA was subcloned into the pGEM-HE vector, the construct was
629 linearized with NheI, and complementary RNA (cRNA) was synthesized by in vitro
630 transcription using T7 RNA polymerase (Thermo Fisher). All defolliculated oocytes were
631 purchased from Ecocyte (Austin, TX). Oocytes were injected with cRNA for each of the constructs
632 and incubated at 17˚C for 1-3 days in a solution containing 96 mM NaCl, 2 mM KCl, 1 mM
633 MgCl2, 1.8 mM CaCl2, 5 mM HEPES, pH 7.6 (with NaOH), and gentamicin. For the two-

634 electrode voltage-clamp recording, oocyte membrane voltage was controlled using an OC-725C
635 oocyte clamp (Warner Instruments). Data were filtered at 1–3 kHz and digitized at 20 kHz using
636 pClamp software (Molecular Devices) and a Digidata 1440A digitizer (Axon Instruments).
637 Microelectrode resistances were 0.1–1 MΩ when filled with 3 M KCl. The external recording
638 solution contained 100 mM KCl, 2 mM $MgCl_2$, 10 mM HEPES, pH 7.6 (with KOH). Agonists,
639 antagonist, and ruthenium red were applied using a gravity-fed perfusion system that can exchange
640 the 150 μL recording chamber volume within a few seconds.
641
642 Antibodies and reagents
643 Primary antibodies used were rabbit anti-Myc (Cell Signaling Technology, 2272), mouse
644 anti-Myc (Cell Signaling Technology, 2276), rabbit anti-GFP (Thermo Fisher Scientific, A-
645 11122), mouse anti-GFP (Thermo Fisher Scientific, A-11120), rabbit anti-RhoA (Cell Signaling
646 Technology, 67B9), Secondary antibodies used were HRP-conjugated monoclonal mouse anti-
647 rabbit IgG, light chain specific (Jackson ImmunoResearch, 211-032-171) and goat anti-rabbit IgG
648 (Li-COR, 926-32211)
649
650 Co-immunoprecipitation
651 HEK293T cells were cultured in Dulbecco's Modified Eagle's Medium (DMEM)
652 supplemented with 10% (vol/vol) fetal calf serum (FCS) and penicillin/streptomycin at 37°C with
653 6% CO2. Cells were transfected with Lipofectamine LTX with Plus Reagent (Thermo Fisher
654 Scientific) and lysed 24 h after transfection in IP Lysis Buffer (Pierce, 25 mM Tris-HCl pH 7.4,
655 150 mM NaCl, 10 mM MgCl2, 1% NP-40, 1 mM EDTA, 5% glycerol) supplemented with EDTA-
656 free Halt protease inhibitor cocktail (Thermo Fisher Scientific). Cells were lysed for 15 min
657 followed by centrifugation at 14,000 RPM for 10 min. Supernatants were incubated with primary
658 antibody bound to magnetic Protein G Dynabeads (Thermo Fisher Scientific) for 1 h at 4°C
659 followed by several washes in IP wash buffer (PBS, 0.2% Tween 20). To elute bound proteins,
660 Laemmli sample buffer with β-mercaptoethanol was added to the beads and samples were heated
661 for 10 min at 70°C. Protein lysates were resolved on 4–15% TGX gels (Bio-Rad Laboratories) and
662 transferred to PVDF membranes. Membranes were developed using SuperSignal West Femto
663 Maximum Sensitivity Substrate (Thermo Fisher Scientific) and imaged using an ImageQuant LAS
664 4000 system (GE Healthcare).
665

666 Calcium imaging

667 MN-1 cells were transfected with TRPV4-GFP (WT or mutant) constructs or co-
668 transfected with TRPV4-GFP and RhoA-Myc (WT or mutant) constructs using Lipofectamine
669 LTX. Calcium imaging was performed on a Zeiss Axio Observer.Z1 inverted microscope equipped
670 with a Lambda DG-4 (Sutter Instrument Company, Novato, CA) wavelength switcher. Cells were
671 bath-loaded with Fura-2 AM (8 μM, Life Technologies) for 45-60 min at 37°C in calcium-imaging
672 buffer (150 mM NaCl, 5 mM KCl, 1 mM MgCl2, 2 mM CaCl2, 10 mM glucose, 10 mM HEPES,
673 pH 7.4). For hypotonic saline treatment, one volumes of NaCl-free calcium-imaging buffer was
674 added to one volume of standard calcium-imaging buffer for a final NaCl concentration of 70 mM.
675 Cells were imaged every 10 sec for 30 sec prior to stimulation with hypotonic saline or GSK101,
676 and then imaged every 10 sec for an additional 2 min. Calcium levels at each time point were
677 computed by determining the ratio of Fura-2 AM emission at 340 nM divided by the emission at
678 380 nM. Data were expressed as Fura ratio over time.

679

680 **Data availability:**

681 Coordinates have been deposited in the Protein Data Bank with the PDB IDs - 8FC9 (TRPV4-
682 RhoA, apo), 8FC7 (TRPV4-RhoA, GSK279-bound closed), 8FCB (TRPV4-RhoA, GSK101
683 bound, open), 8FC8 (TRPV4, GSK101 bound, open), 8FCA (TRPV4, 4α–PDD-bound, putative
684 open) respectively. The cryo-EM maps have been deposited in the Electron Microscopy Data Bank
685 with the IDs EMD - 28977 (TRPV4-RhoA, apo), 28975 (TRPV4-RhoA, GSK279-bound closed),
686 28976 (TRPV4-RhoA and TRPV4 only, GSK101 bound, open), 28978 (TRPV4, 4α–PDD-bound,
687 putative open), respectively.

688

689

690 **Acknowledgements:**

691 Cryo-EM data were screened and collected at the Duke University Shared Materials
692 Instrumentation Facility (SMIF) and at the Pacific Northwest Center for Cryo-EM (PNCC) at
693 OHSU. We thank Nilakshee Bhattacharya at SMIF and Janette Myers at PNCC for assistance with

the microscope operation. We thank Ying Yin and Justin Fedor for critical manuscript reading and advice throughout the project and Yang Suo for assistance in data collection. This research was supported by National Institutes of Health grants R35NS097241 (S.-Y.L.), R35NS122306 (C.J.S) and K08NS102509 (B.A.M.) and Muscular Dystrophy Association 629305 (C.J.S.). A portion of this research was supported by NIH grant U24GM129547 and performed at the PNCC at OHSU and accessed through EMSL (grid.436923.9), a DOE Office of Science User Facility sponsored by the Office of Biological and Environmental Research. DUKE SMIF is affiliated with the North Carolina Research Triangle Nanotechnology Network, which is in part supported by the NSF (ECCS-2025064).

Author Contributions: D.K. conducted biochemical preparation, sample freezing, cryo-EM data collection, and processing, F.Z. conducted biochemical preparation and electrophysiology experiments, all under the guidance of S.-Y.L. D.K. and S.-Y.L. performed model building and refinement. B.A.M, and M.K. carried out immunoprecipitation and calcium imaging experiments under the guidance of C.J.S. S.-Y.L. D.K. C.J.S. B.A.M. J.M.S. and F.Z. wrote the paper.

Competing Interests: The authors declare no competing interests.

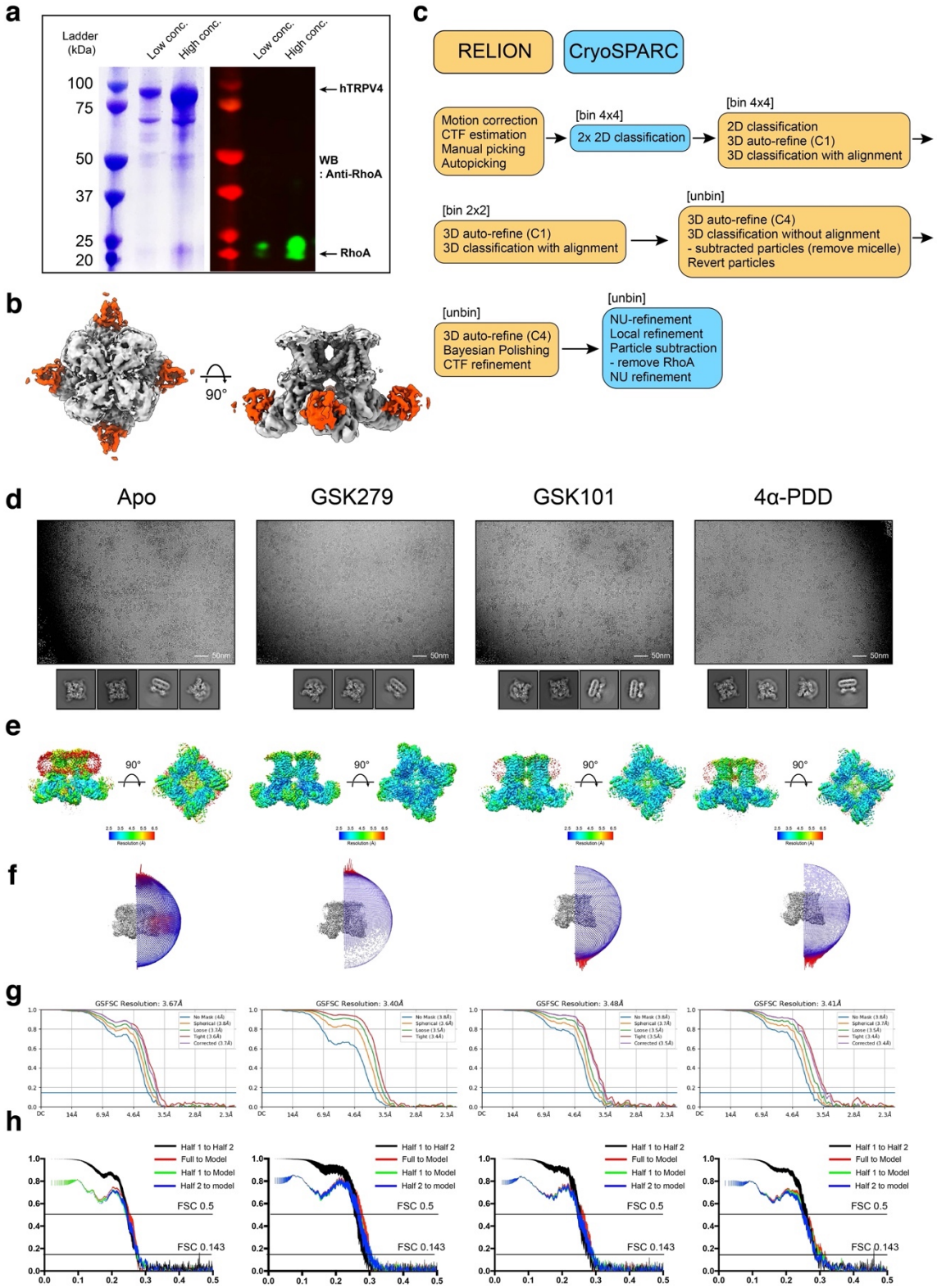

Extended Data Fig. 1. Cryo-EM data processing summary

a, SDS-PAGE and western blot analysis of purified hTRPV4-RhoA.

b, Cryo-EM reconstruction of GSK279-hTRPV4-RhoA imposing symmetry (C1 symmetry). The red-colored densities indicate RhoA binds to each protomer.

c, General cryo-EM data processing procedure. Tasks performed in the RELION software are colored in orange and those in the cryoSPARC in blue.

d, Representative micrographs of hTRPV4-RhoA sample in vitreous ice and 2D classification images.

e, Local resolution estimations.

f, Euler distribution plots.

g, Fourier shell correlation (FSC) curves of the final 3D reconstructions with different masking, as calculated in cryoSPARC.

h, Map-to-model correlation plots for both full maps and half maps.

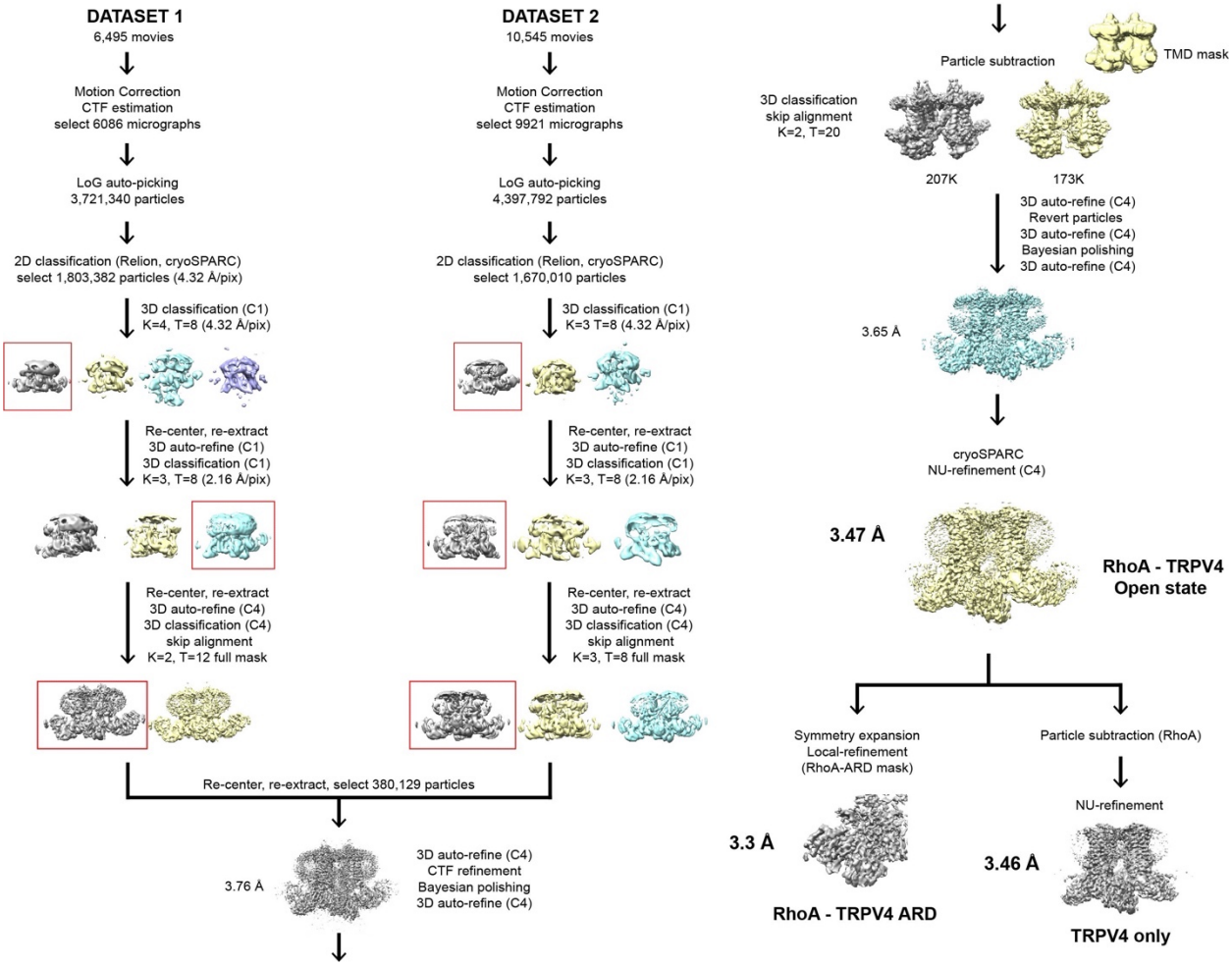

Extended Data Fig. 2. Cryo-EM data processing of the open state (GSK101) structure

The detailed procedure for determining the open state GSK101-hTRPV4-RhoA structure. The final cryo-EM reconstruction at a resolution of 3.47 Å of GSK101-hTRPV4-RhoA, RhoA-ARD focused map at a 3.30 Å, TRPV4 focused map at a 3.46 Å.

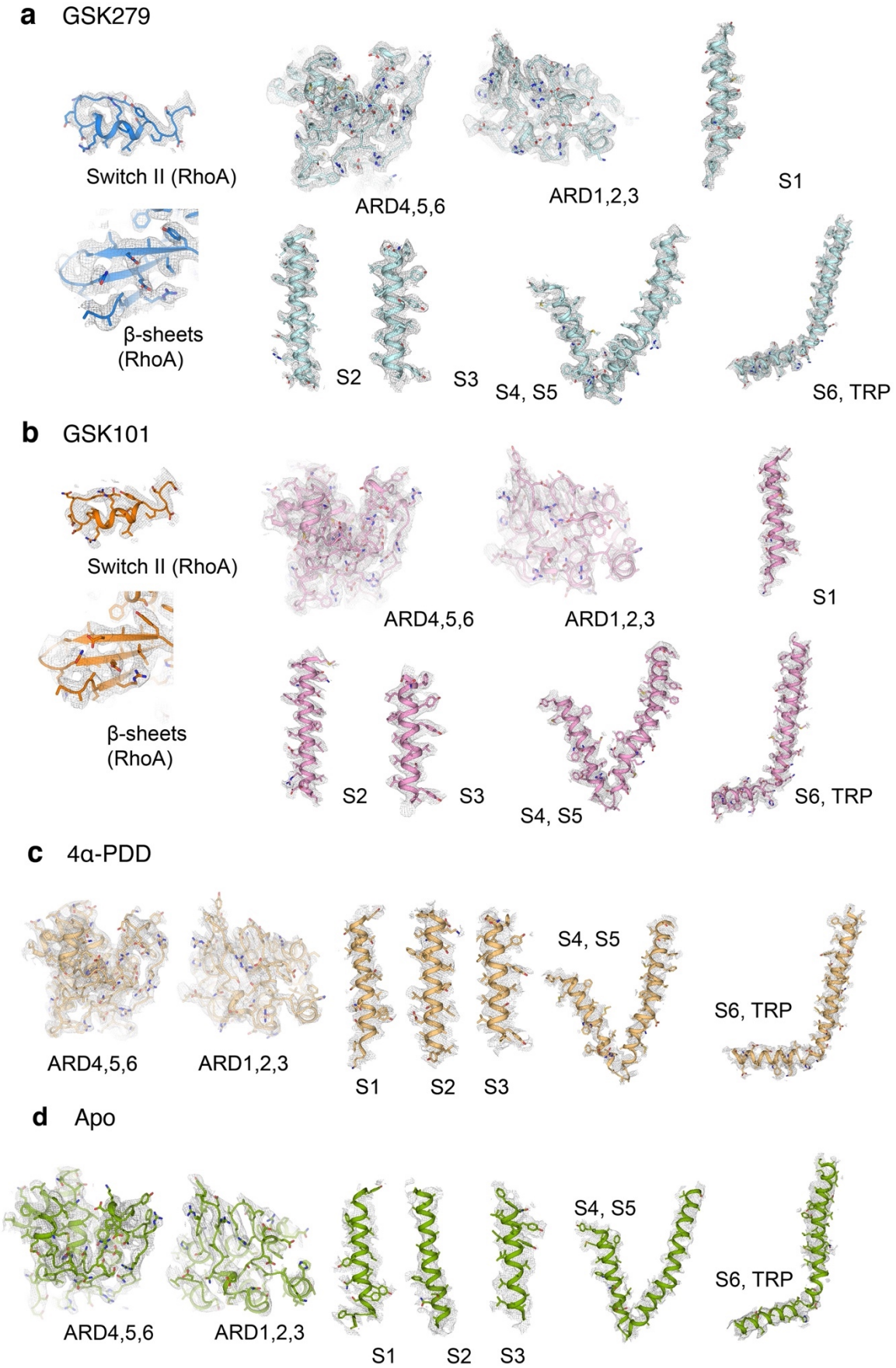
a GSK279
Switch II (RhoA)
ARD4,5,6
ARD1,2,3
S1
β-sheets
(RhoA)
S2
S3
S4, S5
S6, TRP
b GSK101
Switch II (RhoA)
ARD4,5,6
ARD1,2,3
S1
β-sheets
(RhoA)
S2
S3
S4, S5
S6, TRP
c 4α-PDD
ARD4,5,6
ARD1,2,3
S1
S2
S3
S4, S5
S6, TRP
d Apo
ARD4,5,6
ARD1,2,3
S1
S2
S3
S4, S5
S6, TRP

767 **Extended Data Fig. 3. Representative Cryo-EM density of the TRPV4-RhoA structures**

768 **a-d**, Representative cryo-EM densities for various structural elements in the structures of GSK279-
769 hTRPV4-RhoA (**a**, blue and cyan), GSK101-hTRPV4-RhoA (**b**, orange and pink), 4α-PDD-
770 hTRPV4-RhoA, (**c**, light gold), and apo-hTRPV4-RhoA (**d**, green). RhoA densities in the
771 GSK279- and GSK101-bound structures are from the focused-refined maps. EM densities are
772 shown as gray meshes at thresholding of 0.23-0.25, 0.22–0.24, 0.17–0.19, and 0.16–0.18,
773 respectively, in **a-d**.

774
775
776
777
778
779
780
781
782
783
784
785
786
787
788
789
790
791
792
793
794
795

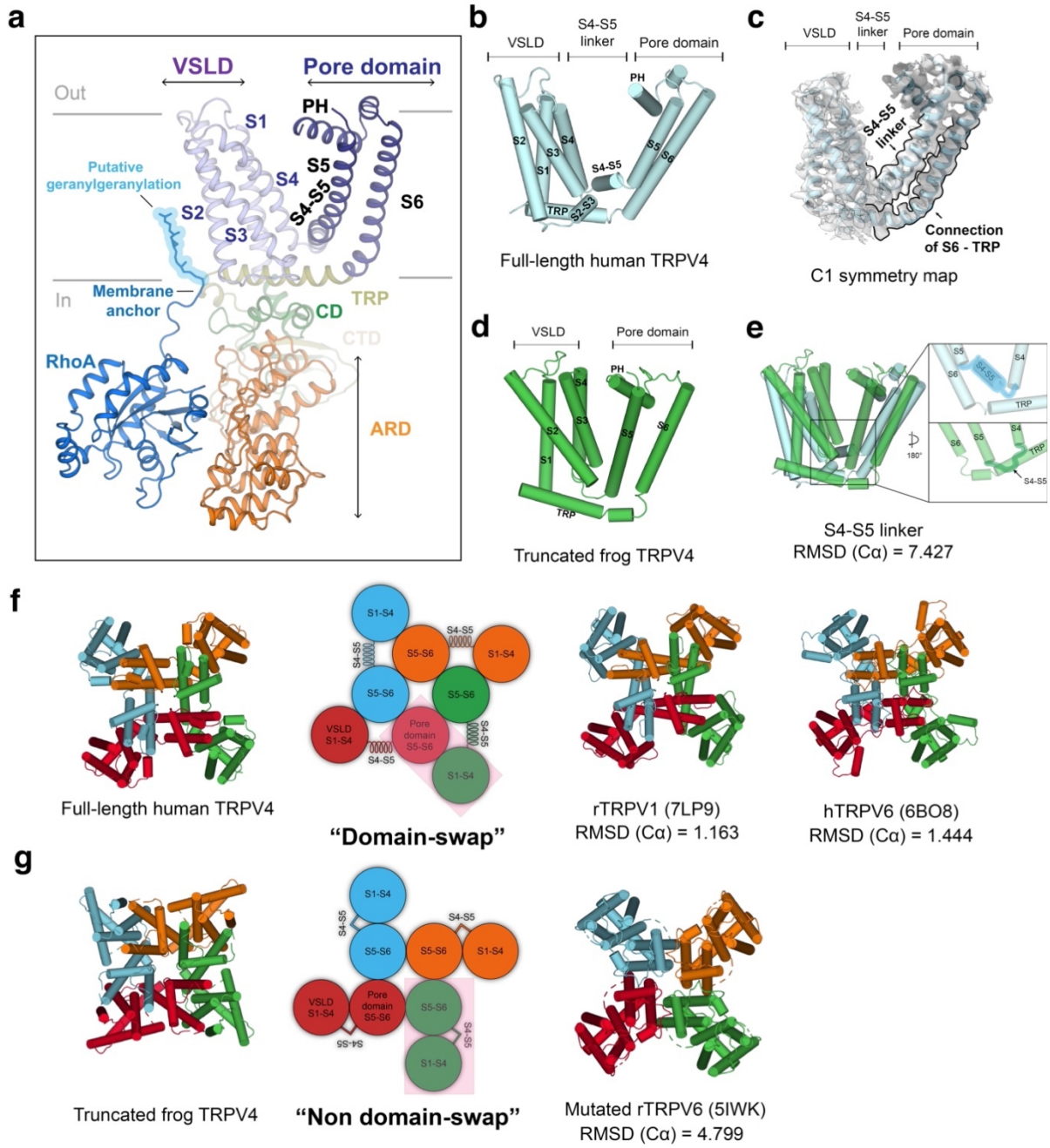

Extended Data Fig. 4. Structural comparisons between human TRPV4 and frog TRPV4

a, Architecture of the hTRPV4 protomer and RhoA with subdomains indicated: ankyrin repeat domain (ARD), coupling domain (CD), transmembrane helices (S1-S6), pore helix (PH), TRP helix, C-terminal domain (CTD), and RhoA. Membrane-anchored lipid tail of RhoA is highlighted in blue.

b, Cylinder representation of the TMD of human TRPV4 in cyan.

c, Cryo-EM density (no imposed symmetry) of GSK279-hTRPV4-RhoA complex for the domain-swapping linkers (S4-S5 and S6-TRP), at thresholding 0.35.

d, Cylinder representation of the TMD of truncated frog TRPV4 in green.

e, Comparison of the TMDs of human TRPV4 and frog TRPV4 viewed from the membrane plane. The linkers between S4 and S5 are highlighted.

f,**g**, Comparison of domain-swapping architectures of human TRPV4, rat TRPV1, human TRPV6 (**f**), truncated frog TRPV4, and mutated rat TRPV6 (**g**).

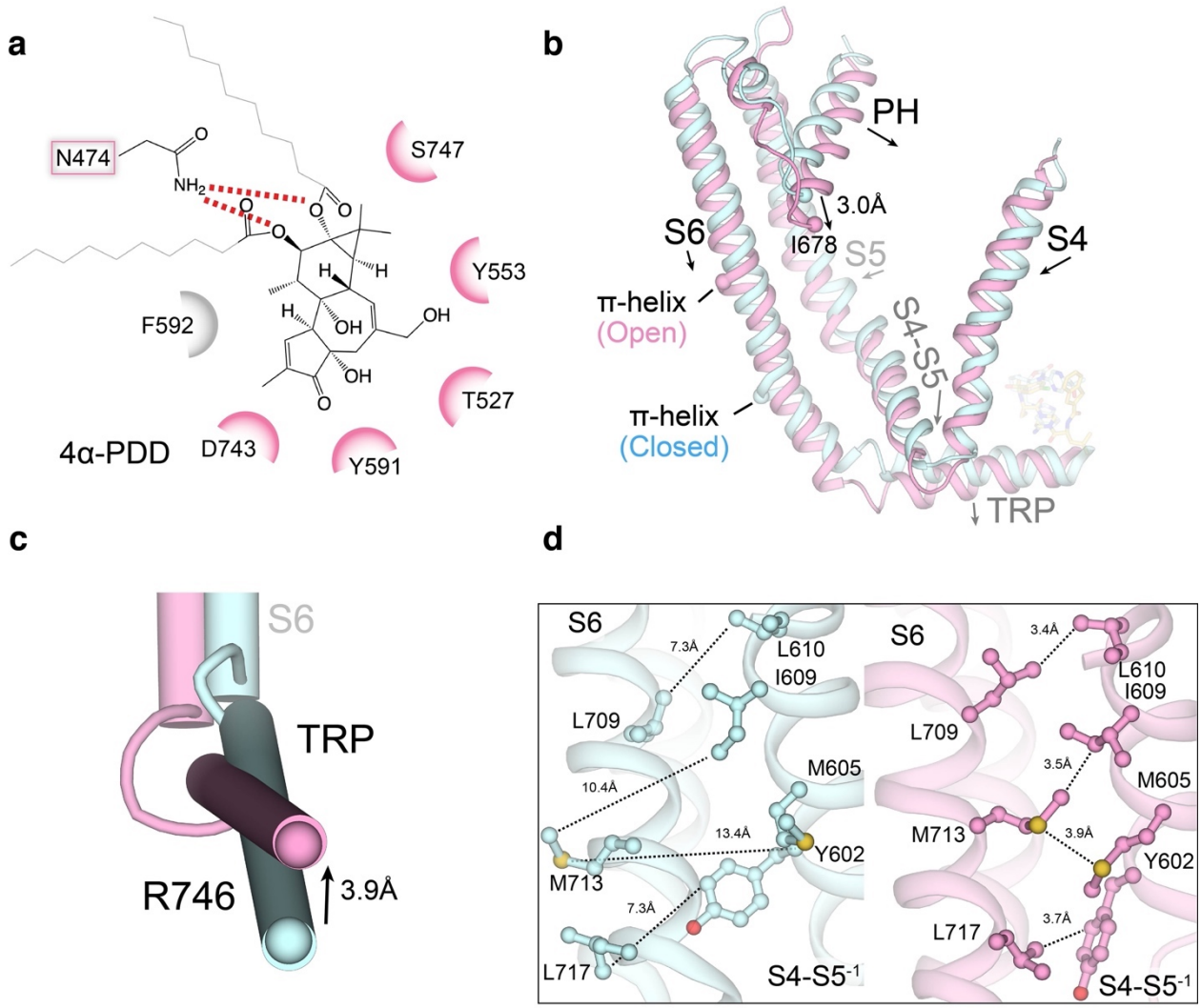

Extended Data Fig. 5. Structural comparison of hTRPV4-RhoA inter- and intra-subunit interfaces in the open and closed states

a, Ligplot[62] schematics of the 4α-PDD interaction with hTRPV4, with key chemical positions labelled. Pink colored residues interact with both GSK101 and GSK279.

b, Comparison of conformational changes at pore-domain of GSK279-hTRPV4-RhoA (cyan) and GSK101-hTRPV4-RhoA (pink). Ligands are shown in sticks. Arrows indicate helix movement with distances indicated between reference points (as spheres).

c, Closed-up view of S6b and the TRP helix. Arrows indicate helical movements with distances indicated between reference points (as spheres).

d, Side-by-side comparison of the closed (cyan) and open states (pink) at inter-subunit interfaces.

Sidechains are shown as sticks. Dashed lines indicate the distances between corresponding residues.

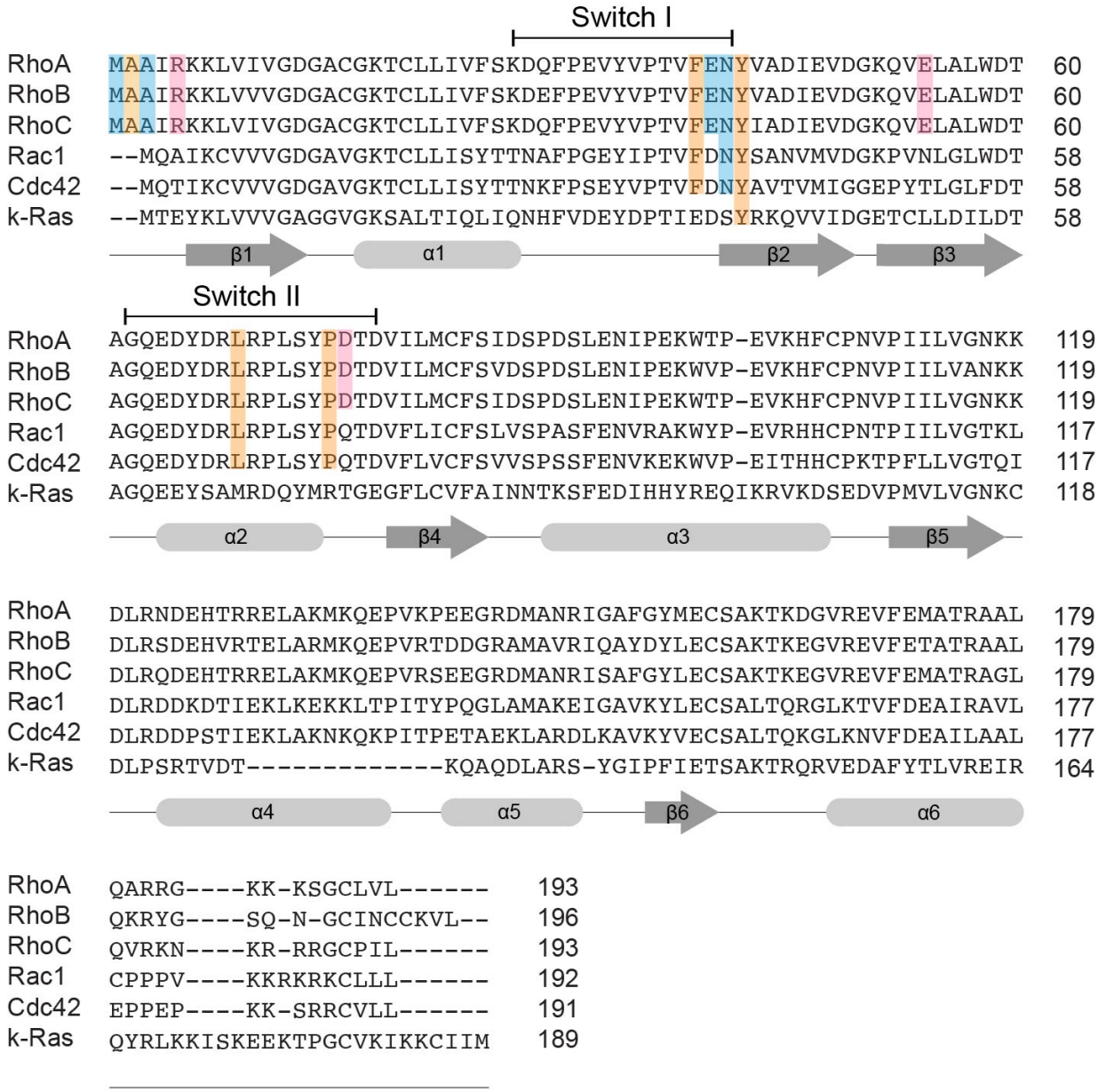

Extended Data Fig. 6. Sequence-alignment of Rho family of GTPases

Secondary structure elements based on RhoA are shown as gray cylinders (helices) and arrows (beta-strand). The RhoA residues critical for interaction are highlighted: blue for backbone - M1, A3, E40, N41, pink for sidechain - R5, E54, D76, and orange for hydrophobic - A2, F39, Y42, L69, P75.

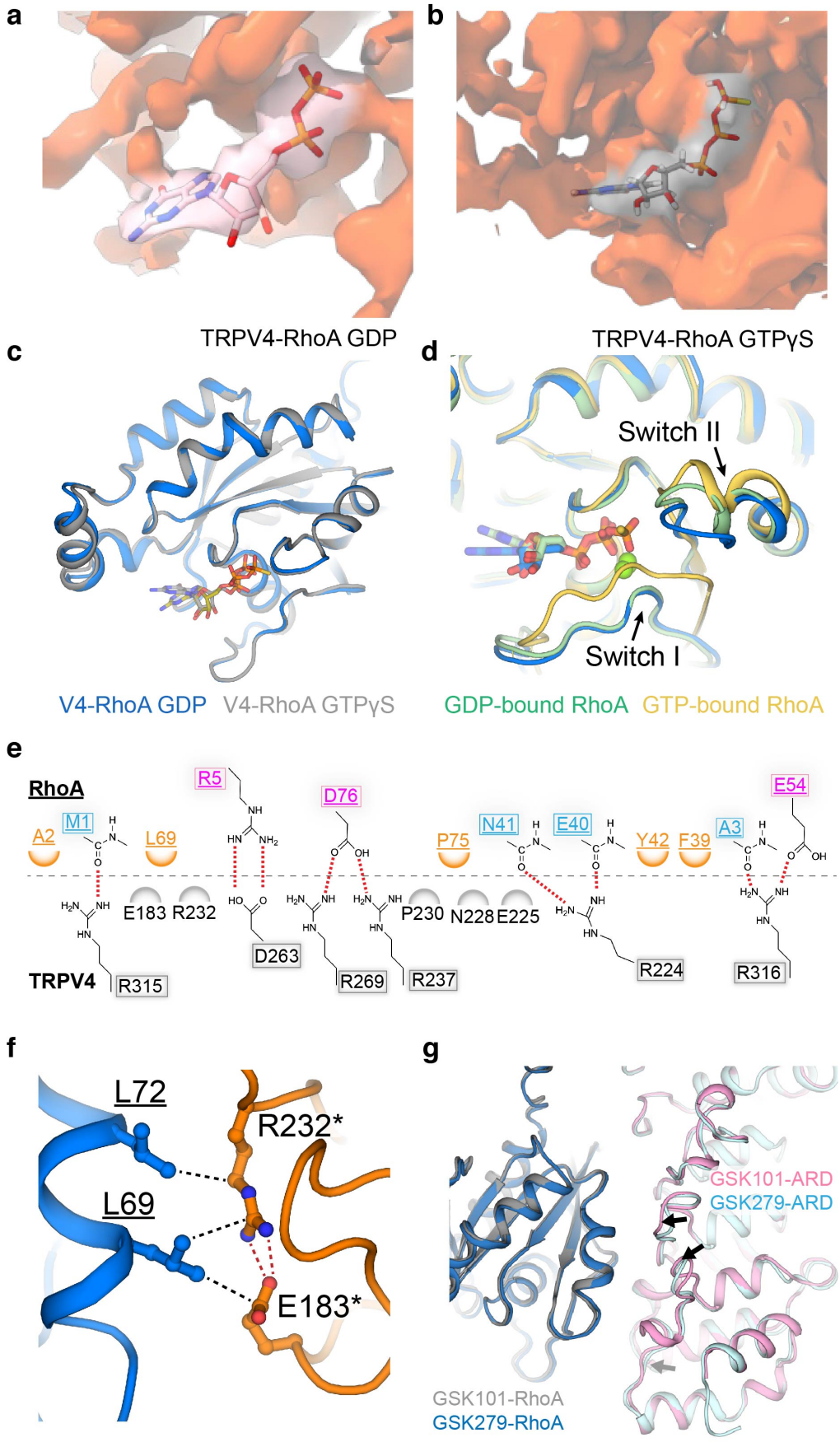
a
b
TRPV4-RhoA GDP
TRPV4-RhoA GTPγS
c
d
Switch II
Switch I
V4-RhoA GDP
V4-RhoA GTPγS
GDP-bound RhoA
GTP-bound RhoA
e
RhoA
A2
M1
L69
R5
D76
P75
N41
E40
Y42
F39
A3
E54
E183
R232
P230
N228
E225
D263
R269
R237
R224
R316
TRPV4
R315
f
L72
L69
R232*
E183*
g
GSK101-ARD
GSK279-ARD
GSK101-RhoA
GSK279-RhoA

890

Extended Data Fig. 7. Structural comparisons of the TRPV4-bound RhoA and published RhoA

a,**b**, Close-up view at the nucleotide binding site in RhoA of 3D reconstructions of GSK279-hTRPV4-RhoA-GDP (**a**) and GSK101-hTRPV4-RhoA-GTPγS (**b**) at thresholding 0.17 and 0.135, respectively. Nucleotides are shown as sticks.

c, Comparison of RhoA conformations of GSK279-hTRPV4-RhoA-GDP and GSK101-hTRPV4-RhoA- GTPγS. Nucleotides are shown as sticks.

d, Comparison of RhoA conformations of GSK279-hTRPV4-RhoA-GDP (blue), GDP-bound RhoA (PDB-1FTN, green), and GTPγS-bound RhoA (PDB-1A2B, gold). Nucleotides are shown as sticks and Magnesium ions are shown as spheres.

e, DIMplot[62] schematics of TRPV4 ARD and RhoA interactions, with critical positions labeled. Pink-colored residues indicate interactions via sidechains. Blue-colored residues indicate backbone-sidechain interactions. Orange-colored residues indicate hydrophobic interactions.

f, Detailed hydrophobic interaction of TRPV4-ARD and RhoA. Underlined residues located in RhoA, and annotated residues indicate disease-causing mutations. The red and black dotted lines indicate salt bridges and hydrophobic interactions, respectively.

g, Comparison of the interaction interface between GSK279-hTRPV4-RhoA-GDP and GSK101-hTRPV4-RhoA-GTPγS. Arrows indicate conformational changes.

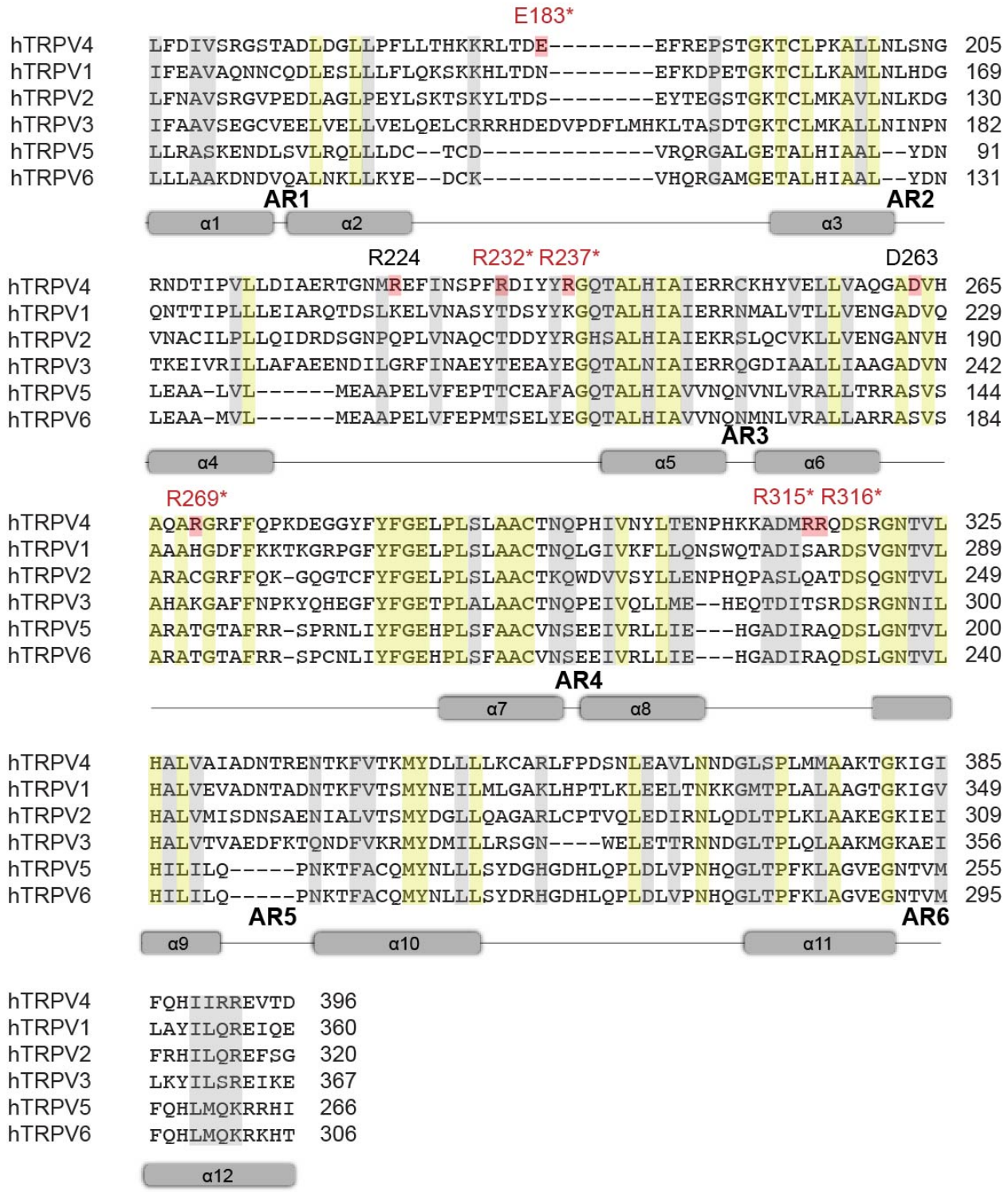

Extended Data Fig. 8. Sequence alignment of the ARDs in human TRPV channels

The α-helices shown as gray cylinders, well-conserved residues highlighted in yellow (identical) and gray (similar), and key residues for TRPV4 interaction are colored in red. Annotated residues are variant positions in neuropathy disease.

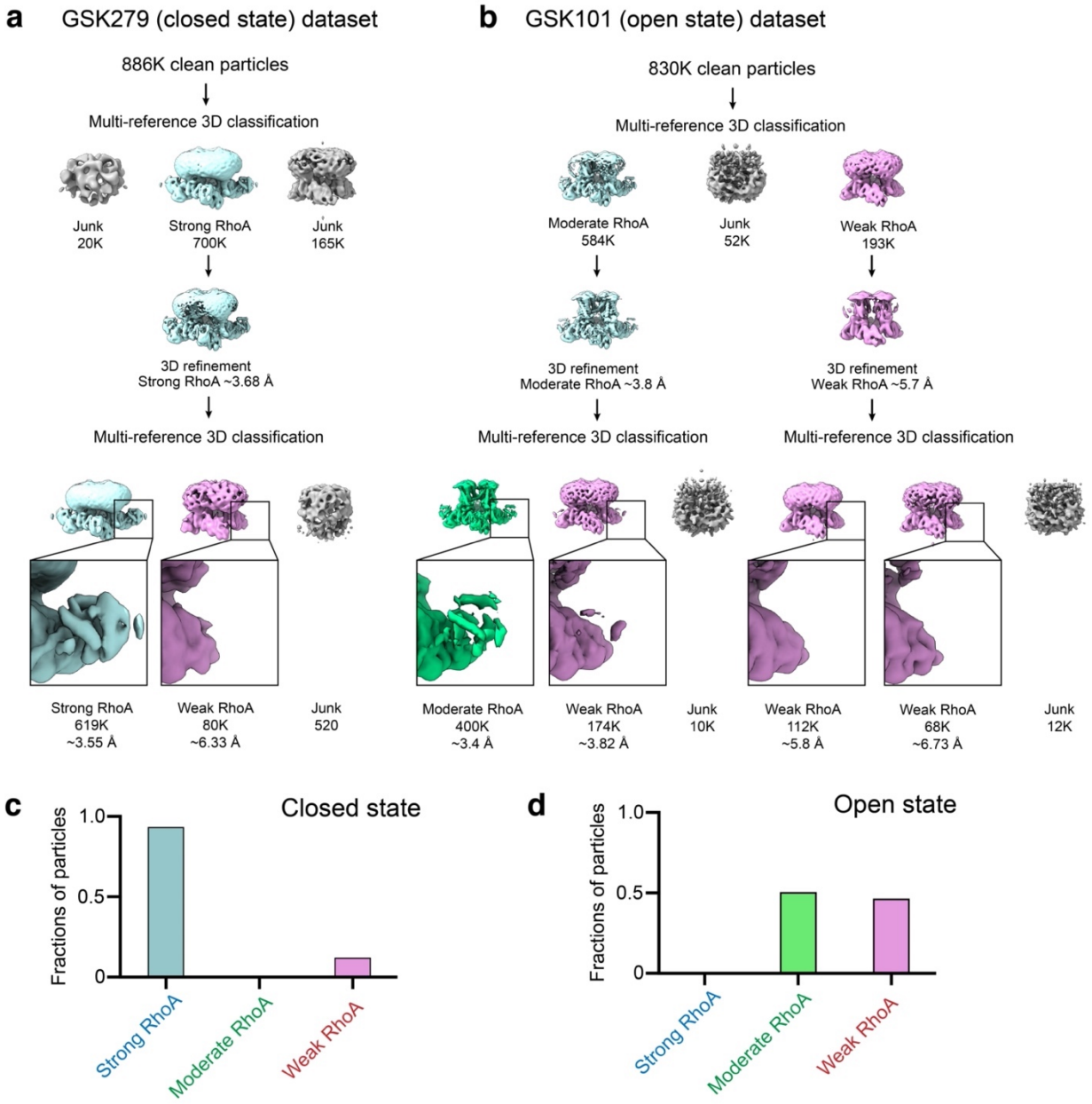

Extended Data Fig. 9. Image processing workflow for the RhoA-bound fraction analysis

a, Data processing workflow of GSK279-hTRPV4-RhoA dataset for the purpose of the RhoA-bound fraction analysis. 3D reconstruction thresholding of 0.58.

b, Data processing workflow of GSK101-hTRPV4-RhoA dataset for the purpose of the RhoA-bound fraction analysis. The red- and blue-outlined subsets indicate the RhoA-bound fraction and RhoA-unbound fraction, respectively. 3D reconstruction thresholding of 0.58.

c, Class distributions of particles for GSK279-hTRPV4-RhoA.

d, Class distributions of particles for GSK101-hTRPV4-RhoA.

References

1. Lavanderos, B. et al. TRP Channels Regulation of Rho GTPases in Brain Context and Diseases. *Frontiers in Cell and Developmental Biology* **8**(2020).
2. Garcia-Elias, A. et al. The TRPV4 channel. *Handb Exp Pharmacol* **222**, 293-319 (2014).
3. White, J.P. et al. TRPV4: Molecular Conductor of a Diverse Orchestra. *Physiol Rev* **96**, 911-73 (2016).
4. Grace, M.S., Bonvini, S.J., Belvisi, M.G. & McIntyre, P. Modulation of the TRPV4 ion channel as a therapeutic target for disease. *Pharmacology & Therapeutics* **177**, 9-22 (2017).
5. Bera, K. et al. Extracellular fluid viscosity enhances cell migration and cancer dissemination. *Nature* (2022).
6. Deng, H.X. et al. Scapuloperoneal spinal muscular atrophy and CMT2C are allelic disorders caused by alterations in TRPV4. *Nature Genetics* **42**, 165-U102 (2010).
7. Landoure, G. et al. Mutations in TRPV4 cause Charcot-Marie-Tooth disease type 2C. *Nature Genetics* **42**, 170-U109 (2010).
8. Lamande, S.R. et al. Mutations in TRPV4 cause an inherited arthropathy of hands and feet. *Nature Genetics* **43**, 1142-U141 (2011).
9. Kang, S.S., Shin, S.H., Auh, C.K. & Chun, J. Human skeletal dysplasia caused by a constitutive activated transient receptor potential vanilloid 4 (TRPV4) cation channel mutation. *Experimental and Molecular Medicine* **44**, 707-722 (2012).
10. Rock, M.J. et al. Gain-of-function mutations in TRPV4 cause autosomal dominant brachyolmia. *Nat Genet* **40**, 999-1003 (2008).
11. Auer-Grumbach, M. et al. Alterations in the ankyrin domain of TRPV4 cause congenital distal SMA, scapuloperoneal SMA and HMSN2C. *Nat Genet* **42**, 160-4 (2010).
12. Cachero, T.G., Morielli, A.D. & Peralta, E.G. The small GTP-binding protein RhoA regulates a delayed rectifier potassium channel. *Cell* **93**, 1077-1085 (1998).
13. Pochynyuk, O., Stockand, J.D. & Staruschenko, A. Ion channel regulation by Ras, Rho, and Rab small GTPases. *Experimental Biology and Medicine* **232**, 1258-1265 (2007).
14. Chinigo, G., Pla, A.F. & Gkika, D. TRP Channels and Small GTPases Interplay in the Main Hallmarks of Metastatic Cancer. *Frontiers in Pharmacology* **11**(2020).
15. Staruschenko, A. et al. Rho small GTPases activate the epithelial Na+ channel. *Journal of Biological Chemistry* **279**, 49989-49994 (2004).
16. Herbert, L.M., Resta, T.C. & Jernigan, N.L. RhoA increases ASIC1a plasma membrane localization and calcium influx in pulmonary arterial smooth muscle cells following chronic hypoxia. *American Journal of Physiology-Cell Physiology* **314**, C166-C176 (2018).
17. Watanabe, H. et al. Anandamide and arachidonic acid use epoxyeicosatrienoic acids to activate TRPV4 channels. *Nature* **424**, 434-438 (2003).
18. Liedtke, W. et al. Vanilloid receptor-related osmotically activated channel (VR-OAC), a candidate vertebrate osmoreceptor. *Cell* **103**, 525-535 (2000).
19. Guler, A.D. et al. Heat-evoked activation of the ion channel, TRPV4. *Journal of Neuroscience* **22**, 6408-6414 (2002).
20. Rosenbaum, T. et al. TRPV4: A Physio and Pathophysiologically Significant Ion Channel. *Int J Mol Sci* **21**(2020).
21. Thoppil, R.J. et al. TRPV4 channels regulate tumor angiogenesis via modulation of Rho/Rho kinase pathway. *Oncotarget* **7**, 25849-25861 (2016).
22. McCray, B.A. et al. Neuropathy-causing TRPV4 mutations disrupt TRPV4-RhoA interactions and impair neurite extension. *Nature Communications* **12**(2021).
23. Goyal, N. et al. Clinical Pharmacokinetics, Safety, and Tolerability of a Novel, First-in-Class TRPV4 Ion Channel Inhibitor, GSK2798745, in Healthy and Heart Failure Subjects. *American Journal of Cardiovascular Drugs* **19**, 335-342 (2019).
24. Thorneloe, K.S. et al. An Orally Active TRPV4 Channel Blocker Prevents and Resolves Pulmonary Edema Induced by Heart Failure. *Science Translational Medicine* **4**(2012).
25. Liu, M.Y. et al. TRPV4 Inhibition Improved Myelination and Reduced Glia Reactivity and Inflammation in a Cuprizone-Induced Mouse Model of Demyelination. *Frontiers in Cellular Neuroscience* **12**(2018).
26. Arredondo Zamarripa, D. et al. Dual contribution of TRPV4 antagonism in the regulatory effect of vasoinhibins on blood-retinal barrier permeability: diabetic milieu makes a difference. *Sci Rep* **7**, 13094 (2017).

27. Deng, Z.Q. et al. Cryo-EM and X-ray structures of TRPV4 reveal insight into ion permeation and gating mechanisms. *Nature Structural & Molecular Biology* **25**, 252-+ (2018).
28. Huffer, K.E., Aleksandrova, A.A., Jara-Oseguera, A., Forrest, L.R. & Swartz, K.J. Global alignment and assessment of TRP channel transmembrane domain structures to explore functional mechanisms. *Elife* **9**(2020).
29. Hu, H., Grandl, J., Bandell, M., Petrus, M. & Patapoutian, A. Two amino acid residues determine 2-APB sensitivity of the ion channels TRPV3 and TRPV4. *Proc Natl Acad Sci U S A* **106**, 1626-31 (2009).
30. Zubcevic, L., Borschel, W.F., Hsu, A.L., Borgnia, M.J. & Lee, S.Y. Regulatory switch at the cytoplasmic interface controls TRPV channel gating. *Elife* **8**(2019).
31. Vriens, J., Owsianik, G., Janssens, A., Voets, T. & Nilius, B. Determinants of 4 alpha-phorbol sensitivity in transmembrane domains 3 and 4 of the cation channel TRPV4. *Journal of Biological Chemistry* **282**, 12796-12803 (2007).
32. Donate-Macian, P. et al. Structural determinants of TRPV4 inhibition and identification of new antagonists with antiviral activity. *Br J Pharmacol* **179**, 3576-3591 (2022).
33. Voets, T. et al. Molecular determinants of permeation through the cation channel TRPV4. *Journal of Biological Chemistry* **277**, 33704-33710 (2002).
34. Zubcevic, L. & Lee, S.Y. The role of pi-helices in TRP channel gating. *Curr Opin Struct Biol* **58**, 314-323 (2019).
35. Schaefer, A., Reinhard, N.R. & Hordijk, P.L. Toward understanding RhoGTPase specificity: structure, function and local activation. *Small GTPases* **5**, 6 (2014).
36. Kakiuchi, M. et al. Recurrent gain-of-function mutations of RHOA in diffuse-type gastric carcinoma. *Nature Genetics* **46**, 583-587 (2014).
37. Schaefer, A. & Der, C.J. RHOA takes the RHOad less traveled to cancer. *Trends Cancer* **8**, 655-669 (2022).
38. Porter, A.P., Papaioannou, A. & Malliri, A. Deregulation of Rho GTPases in cancer. *Small GTPases* **7**, 123-38 (2016).
39. Li, X.C. et al. Calcium and TRPV4 promote metastasis by regulating cytoskeleton through the RhoA/ROCK1 pathway in endometrial cancer. *Cell Death & Disease* **11**(2020).
40. Kwon, D., Zhang, F., Fedor, J.G., Suo, Y. & Lee, S.Y. Vanilloid-dependent TRPV1 opening trajectory from cryoEM ensemble analysis. *Nature Communications* **13**(2022).
41. Bagnell, A.M., Sumner, C.J. & McCray, B.A. TRPV4: A trigger of pathological RhoA activation in neurological disease. *Bioessays* **44**(2022).
42. Lakk, M. & Krizaj, D. TRPV4-Rho signaling drives cytoskeletal and focal adhesion remodeling in trabecular meshwork cells. *American Journal of Physiology-Cell Physiology* **320**, C1013-C1030 (2021).
43. Wood, J.M. Osmosensing by bacteria: signals and membrane-based sensors. *Microbiol Mol Biol Rev* **63**, 230-62 (1999).
44. Peng, F.F. et al. Mechanical stretch-induced RhoA activation is mediated by the RhoGEF Vav2 in mesangial cells. *Cellular Signalling* **22**, 34-40 (2010).
45. Becker, D., Bereiter-Hahn, J. & Jendrach, M. Functional interaction of the cation channel transient receptor potential vanilloid 4 (TRPV4) and actin in volume regulation. *Eur J Cell Biol* **88**, 141-52 (2009).
46. Goehring, A. et al. Screening and large-scale expression of membrane proteins in mammalian cells for structural studies. *Nat Protoc* **9**, 2574-85 (2014).
47. Kimanius, D., Dong, L., Sharov, G., Nakane, T. & Scheres, S.H.W. New tools for automated cryo-EM single-particle analysis in RELION-4.0. *Biochemical Journal* **478**, 4169-4185 (2021).
48. Punjani, A., Rubinstein, J.L., Fleet, D.J. & Brubaker, M.A. cryoSPARC: algorithms for rapid unsupervised cryo-EM structure determination. *Nat Methods* **14**, 290-296 (2017).
49. Zheng, S.Q. et al. MotionCor2: anisotropic correction of beam-induced motion for improved cryo-electron microscopy. *Nat Methods* **14**, 331-332 (2017).
50. Zhang, K. Gctf: Real-time CTF determination and correction. *J Struct Biol* **193**, 1-12 (2016).
51. Zivanov, J., Nakane, T. & Scheres, S.H.W. Estimation of high-order aberrations and anisotropic magnification from cryo-EM data sets in RELION-3.1. *IUCrJ* **7**, 253-267 (2020).
52. Zivanov, J., Nakane, T. & Scheres, S. A Bayesian approach to beam-induced motion correction in cryo-EM single-particle analysis. *bioRxiv* (2018).
53. Punjani, A., Zhang, H. & Fleet, D.J. Non-uniform refinement: adaptive regularization improves single-particle cryo-EM reconstruction. *Nature Methods* **17**, 1214-1221 (2020).
54. Emsley, P. & Cowtan, K. Coot: model-building tools for molecular graphics. *Acta Crystallogr D Biol Crystallogr* **60**, 2126-32 (2004).

55. Moriarty, N.W., Grosse-Kunstleve, R.W. & Adams, P.D. electronic Ligand Builder and Optimization Workbench (eLBOW): a tool for ligand coordinate and restraint generation. *Acta Crystallogr D Biol Crystallogr* **65**, 1074-80 (2009).
56. Adams, P.D. et al. PHENIX: a comprehensive Python-based system for macromolecular structure solution. *Acta Crystallogr D Biol Crystallogr* **66**, 213-21 (2010).
57. Chen, V.B. et al. MolProbity: all-atom structure validation for macromolecular crystallography. *Acta Crystallogr D Biol Crystallogr* **66**, 12-21 (2010).
58. Afonine, P.V. et al. New tools for the analysis and validation of cryo-EM maps and atomic models. *Acta Crystallographica Section D-Structural Biology* **74**, 814-840 (2018).
59. Delano, W.L. *The PyMol Molecular Graphics System*, (DeLano Scientific, Palo Alto, CA, USA, 2002).
60. Goddard, T.D., Huang, C.C. & Ferrin, T.E. Visualizing density maps with UCSF Chimera. *J Struct Biol* **157**, 281-7 (2007).
61. Pettersen, E.F. et al. UCSF ChimeraX: Structure visualization for researchers, educators, and developers. *Protein Sci* **30**, 70-82 (2021).
62. Wallace, A.C., Laskowski, R.A. & Thornton, J.M. Ligplot - a Program to Generate Schematic Diagrams of Protein Ligand Interactions. *Protein Engineering* **8**, 127-134 (1995).